Theses and Dissertations

Student Graduate Works

3-11-2011

Neutron Detection Using Gadolinium-Based Diodes

Benjamin R. Thomas

Follow this and additional works at: https://scholar.afit.edu/etd

Part of the Nuclear Commons

NEUTRON DETECTION USING GADOLINIUM-BASED DIODES

THESIS

Benjamin R. Thomas, Major, USA

AFIT/GNE/ENP/11-M18

DEPARTMENT OF THE AIR FORCE

AIR UNIVERSITY

AIR FORCE INSTITUTE OF TECHNOLOGY

Wright-Patterson Air Force Base, Ohio

AFIT/GNE/ENP/11-M18

NEUTRON DETECTION USING GADOLINIUM-BASED DIODES

THESIS

Presented to the Faculty

Department of Engineering Physics

Graduate School of Engineering and Management

Air Force Institute of Technology

Air University

Air Education and Training Command

In Partial Fulfillment of the Requirements for the

Degree of Master of Science in Nuclear Engineering

Benjamin R. Thomas, BS

Major, USA

March 2011

AFIT/GNE/ENP/11-M18

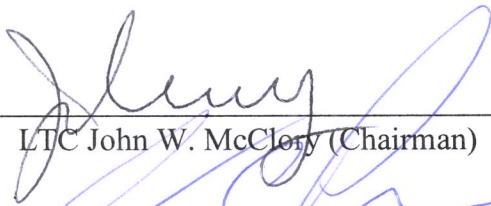# NEUTRON DETECTION USING GADOLINIUM-BASED DIODES
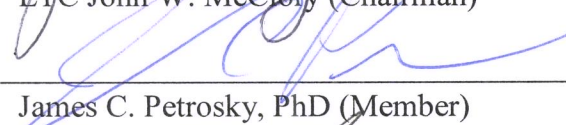
Benjamin R. Thomas, BS

Major, USA

Approved:

_____
LTC John W. McClory (Chairman)

4 Mar 11
Date

_____
James C. Petrosky, PhD (Member)

01 Mar 11
Date

_____
Maj. Benjamin R. Kowash (Member)

04 Mar 11
Date

Abstract

P-n heterojunction diodes consisting of a thin n-type layer of Gd_2O_3 deposited on both p-type Si and p-type 4H SiC substrates were explored as possible solid-state neutron detectors. 79 keV internal conversion electrons from the de-excitation of the meta-stable Gd-158 nucleus can create ionization in the depletion region of the reverse-biased diodes resulting in a detectable signal. The diodes were modeled with Davinci software to determine the feasibility of signal detection above the reverse-bias leakage current. A CASINO simulation showed that less than one percent of the internal conversion electrons deposit their full energy within the achievable depletion region. After depositing contacts on samples prepared at the University of Nebraska, Lincoln, the diodes were exposed to thermal neutron fluxes of approximately 10^3 n/cm^2·s in the AFIT Standard Graphite Pile and 10^9 n/cm^2·s in the thermal column of the Ohio State University Research Reactor. Pulse height spectra collected during irradiations at various reverse bias voltages ranging from -0.5 V to -5.0 V revealed no discernable neutron induced features. Oscilloscope traces captured during the high thermal neutron flux irradiations show pulses; however, no evidence exists to attribute these pulses to neutron interactions.

Acknowledgements

For my family

Table of Contents

List of Figures

List of Tables

List of Terms and Abbreviations

AFIT	Air Force Institute of Technology
AFRL	Air Force Research Lab
AGOT	Nuclear Reactor Grade Graphite
BNC	Bayonet Neill-Concelman Coaxial Cable Connector
CASINO	Monte Carlo Simulation of Electron Trajectory in Solids
Cd	Cadmium
C-V	Capacitance versus Voltage
e-h Pair	Electron-Hole Pair
ENDF	Evaluated Nuclear Data File
GEANT4	Geometry and Tracking Software
Gd	Gadolinium
Gd_2O_3	Gadolinium Oxide
HfO_2	Halfnium Oxide
IC	Internal Conversion Electron
I-V	Current versus Voltage
LET	Linear Energy Transfer
MCNP5	Monte Carlo N-Particle Transport Code
OSURR	The Ohio State University Research Reactor
PLD	Pulsed Laser Deposition
PMT	Photo Multiplier Tube
Pu	Plutonium
RFID	Radio Frequency Identification
RRD	Reaction Rate Density
SEM	Scanning Electron Microscope
Si	Silicon
SiC	Silicon Carbide
SNM	Special Nuclear Material
U	Uranium
UNL	The University of Nebraska, Lincoln
XRD	X-Ray Diffraction

NEUTRON DETECTION USING GADOLINIUM-BASED DIODES

I. INTRODUCTION

Since the employment of the first nuclear weapons at Hiroshima and Nagasaki, the threat of attack with weapons employing nuclear technologies has held a prominent place in the minds of the public. The mere mention of a potential nuclear attack or accident can strike terror in the heart of even the most rational mind. In modern society, the possibility of a terrorist strike employing nuclear weapons puts nuclear weapon fuel and possible weapon component detection at the forefront of the homeland security objectives. Special nuclear material (SNM) is defined by Title I of the Atomic Energy Act of 1954 as plutonium, uranium-233, or uranium enriched in the isotopes of uranium-233 or uranium-235 [1]. Table 1 gives a listing of the spontaneous neutron emission rate of the most common forms of SNM.

While the different forms of SNM have a definite energy emission signature, much of this energy can be shielded from current detectors deployed along the borders and at various points of entry to the country. The shielding of SNM is so readily accomplished that when asked by a senator in a closed session with what tool he would use to find an atomic bomb hidden in a city, J. Robert Oppenheimer replied "a screwdriver" [5]. The relative ease of shielding and transportation of SNM across our

borders among seemingly innocuous cargo demands the development of innovative means for detecting the materials required to assemble a nuclear weapon.

Table 1.   The half-lives, primary decay modes, and spontaneous fission neutron emission rates for selected isotopes of special nuclear material [2][3][4].

	Half-Life [years]	Primary Decay Mode	Spontaneous Fission Neutron Emission Rate [n/100 g s]
^{239}Pu	2.41×10^4	α	2
^{240}Pu	6.57×10^3	α	1.38×10^5
^{241}Pu	14.4	β^-	23
^{235}U	7.04×10^8	α	0.14
^{238}U	4.50×10^9	α	1.5

While such a detector has applications outside of homeland security, the overarching goal is to secure our population from domestic detonation of a nuclear device. That said, within the scope of homeland security objectives, there exist myriad applications for such technology. A small, rugged detector with a low power requirement, for example, could be incorporated into the radio frequency identification (RFID) tags attached to shipping containers at their port of embarkation. At each stop along their journey, the RFID tags could be queried to allow the shipper and receiver to track the cargo. If a neutron detector contributed a small component of the RFID signal, then customs officials at the point of entry or earlier check-points en-route have an additional means of discrimination among the vast quantities of shipping containers.

Thus, the motivation for this research is to contribute to on-going efforts to further neutron detection technology.

Research Hypothesis

A solid-state detector composed of a heterojunction diode made from a thin film of gadolinium oxide (Gd_2O_3) and silicon (Si) or silicon carbide (SiC) will detect neutrons.

To determine the validity of this hypothesis, a series of objectives were devised following the well established research philosophy of overlapping emphasis on exploration of theory, modeling, and experiment [12]. Initially, the supporting theory and physics of the detector configuration and the choice of materials employed in its construction were explored. Concurrently, the detector and its constituent materials were modeled using various computer software to provide a feasibility assessment of the mechanisms involved in creating a signal within the detector. Following assembly, the measured characteristics were compared to the model's predictions. The modeling results allowed for manipulation of various parameters during subsequent iterations of device construction to achieve optimal characteristics. Finally, the detector was exposed to various thermal neutron flux environments in an effort to attain a signal attributable to thermal neutron interaction with a gadolinium nucleus.

II. BACKGROUND

2.1 Neutron Detection

Active radiation detectors rely on the interaction of radiation with the detector materials to produce a signal that is then collected and measured. A primary means of signal generation is through measurement of the movement of ions or elementary particles liberated during ionization of detector materials. However, since neutrons are neutral particles and cannot directly produce ionization, the energetic products of a nuclear reaction are typically employed to generate the detection signal. Table 2 lists the most commonly exploited reactions for neutron detection.

As one of the earliest means of detecting radiation, scintillators, utilize materials that emit light when energetic charged particles interact with the constituent atoms. Scintillators engineered for neutron detection typically employ the respective nuclear reactions listed in Table 2. As ionizing particles traverse the bulk of the scintillator, a portion of their energy is used to excite electrons from the valence band into the conduction band. These electrons de-excite by phonon interaction or lattice heating and eventually are trapped at engineered trap sites with energies in the forbidden region between the valence and conduction bands [27]. As the atoms de-excite from the trap site energy level back to the valence band, their remaining excess energy is released as a photon. The intensity of light emitted by this de-excitation process is proportional to the energy deposited [6]. As the scintillation photons leave the crystal, they are typically directed by the detector casing into a photomultiplier tube (PMT). A photocathode at the junction of the detector housing and the PMT converts the photons to electrons, which

4

are subsequently multiplied by a series of dynodes. While they are subject to statistical

fluxuations at low photon intensity and utility limiting size, scintillators remain a staple

of radiation detection technology.

Table 2. A listing of nuclear reactions commonly exploited for neutron detection, the detector technologies employing these reactions, and the neutron capture cross-section of the principle elements of each reaction[3][6].

Detector Technology	Reaction	Cross-Section [barns]
BF$_3$ Proportional Gas Tube Detector Boron Lined Proportional Counter Boron Loaded Scintillator	$^{10}_{5}B + ^{1}_{0}n \rightarrow ^{7}_{3}Li + ^{4}_{2}\alpha$	3840
Lithium Scintillators	$^{6}_{3}Li + ^{1}_{0}n \rightarrow ^{3}_{1}H + ^{4}_{2}\alpha$	940
^{3}He Proportional Counters	$^{3}_{2}He + ^{1}_{0}n \rightarrow ^{3}_{1}H + ^{1}_{1}p$	5330

Somewhat analogous to the multiplication of secondary electrons by the dynodes

in the PMT, proportional counters rely on the acceleration of electrons to produce the

detection signal. For detection, charged particles interact with the atoms of the detector

material and liberate electrons through ionization. In the case of neutron sensitive

proportional counters, the charged particles result as a secondary process from the

reactions listed in Table 2. The ions and free electrons are then accelerated under the

influence of an electric field to the respective oppositely charged electrodes. Typically, a

wire anode runs through the center of a gas filled tube which serves as the cathode as

illustrated in Figure 1.
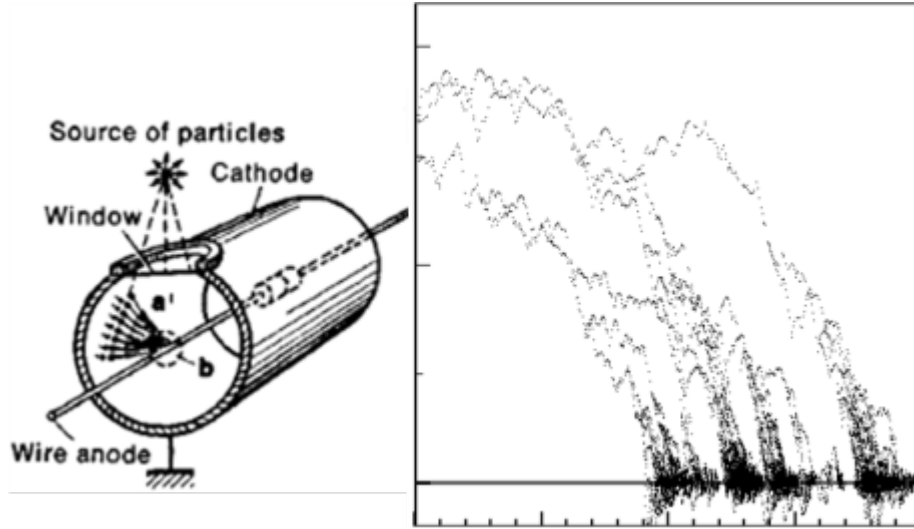
Figure 1. The Gas Proportional Counter. The coaxial geometry (left) of the electrodes creates an electric field sufficient to cause electrons attracted toward the anode to create more e-h pairs. This "avalanche" process (right) is enhanced by engineered fill gases [19][20].

Due to the coaxial nature of the electrode configuration, the electric field, ε, in the volume is given by

$$\varepsilon(r) \propto \frac{V}{r},$$ (1)

where V represents the applied voltage and r the radius. Electrons accelerated toward the anode gain energy sufficient to create further ionizations. Those subsequent electrons from these secondary ionizations are also quickly accelerated toward the anode, causing further ionizations. This process, known as the Townsend avalanche, is enhanced by engineered fill gases [6]. Electron multiplication continues until all of the electrons are collected on the anode, as illustrated in Figure 1.

Similarly, solid-state radiation detectors rely on the ionization of detector materials to create the charge carriers whose movement creates a measureable electronic signal. Solid-state detectors consist of semiconductor diodes reverse-biased to allow

6

minimal current flow while creating an intense electric field in the active detector volume. As ionizing radiation or energetic charged particles pass through the semiconductor and deposit their energy, electrons in the valence band of the semiconductor atoms are excited into the conduction band. Thus, an electron-hole (e-h) pair is created as the electron leaves a vacancy in the valence band to fill a position in the conduction band. While a hole is defined as the absence of an electron, the hole can be thought of as a positive charge carrier. The electron and the hole are then subjected to the electric field, which separates the pair and creates a current as they are swept toward their respective electrodes.

While the same principle of interaction to create a signal is present in all types of radiation detectors, solid-state detectors offer several advantages over other detector technologies. As their name implies, the materials used in solid-state detectors are solids, and thus, have a greater density than proportional counters. This greater density allows for more interactions per volume, and, therefore, a smaller active detector volume. Additionally, the energy required to ionize a semiconductor is generally less than the energy required to ionize an atom of typical fill gases. Figure 1 depicts the relationship between the energy bands of various types of materials. This lower ionization energy of semiconductors translates to the generation of more charge carriers. Therefore, solid-state detectors are subject to less statistical fluxuation when detecting lower energy radiation and are capable of achieving better resolution [6].
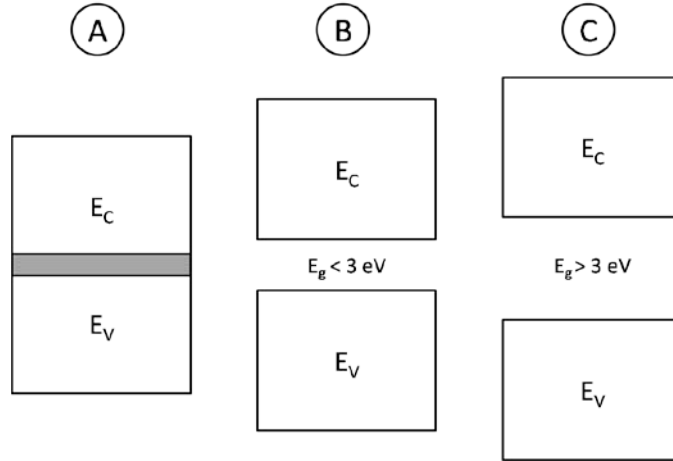
Figure 2. A simplistic depiction of the relationship between the energy bands of different classes of materials. E_C represents the conduction band, while E_V represents the valence band. E_g is the energy gap between the conduction band and the valence band. (A) shows the overlapping energy bands of a typical conductor material. Semiconductors typically have and energy gap of less than 3 eV as shown in (B). Insulator materials have a greater energy gap as shown in (C).

2.2 Properties of Gadolinium

A plot of the total neutron cross-section of elements most commonly used in neutron detection is depicted in Figure 3. The total neutron cross-sections obtained from the Evaluated Nuclear Data File (ENDF) retrieval and plotting tool of the National Nuclear Data Center are plotted for three isotopes of Gadolinium in Figure 4. Gd-157 has the largest-cross section for thermal neutrons of all known natural elements. With a thermal neutron capture cross-section of 255,000 barns, Gd-157 is a natural candidate for utilization as a neutron detector material.
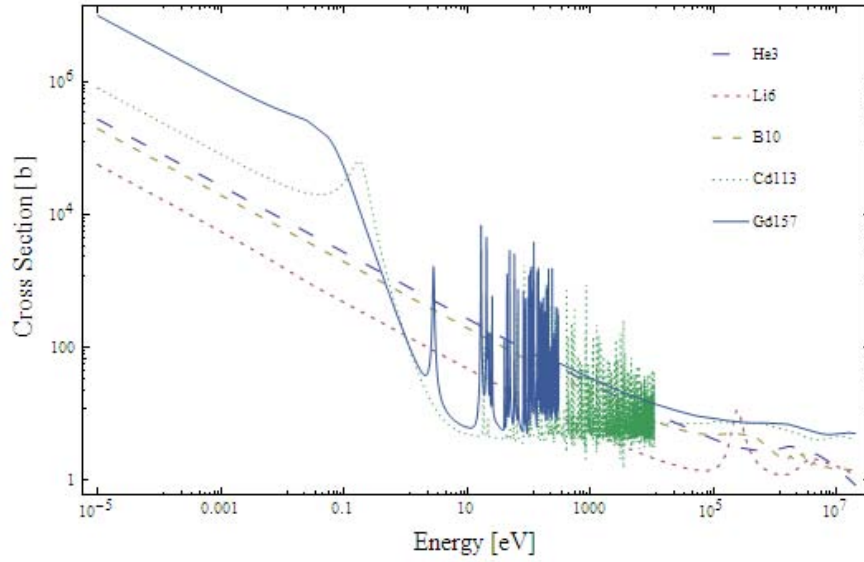
Figure 3. Total neutron cross-section as a function of energy for the elements commonly used in neutron detector technologies. The drop in cross-section just below 1 eV is commonly referred to as the Cadmium cut-off. The cross-section is given in units of barns, where 1 barn=10^{-24} cm^2 [7].
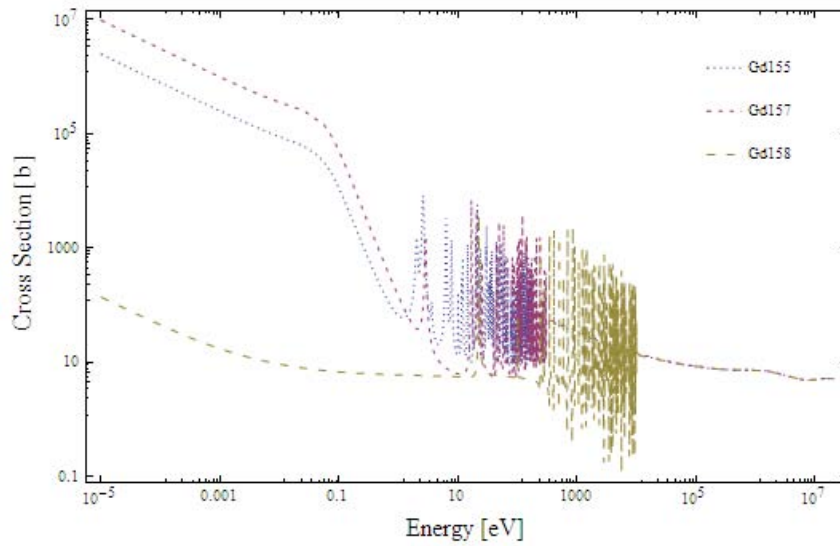
Figure 4. ENDF plot of the total neutron cross-section as a function of energy of three isotopes of Gadolinium. Gd-157 has the highest thermal neutron total cross-section of 255,000 b [7].

Upon absorption of a neutron by the Gd-157 nucleus, the meta-stable Gd-158 nucleus may undergo a myriad of de-excitation schemes to achieve the ground state. One such de-excitation scheme is depicted as

$$^{157}_{64}Gd + ^{1}_{0}n \rightarrow ^{158}_{64}Gd^* \rightarrow \gamma + IC. \qquad (2)$$

The internal conversion (IC) electrons listed in (2) can serve as ionizing particles detectable by various radiation detection technologies. These IC electrons, specifically the 79 keV electron, serve as the basis for this research effort.

Table 3. Listing of the isotopic composition of naturally occurring Gadolinium in weight percentage, the respective half-life of each isotope, and the thermal neutron total cross-section [3][7][8].

	Natural Abundance [weight %]	Half-Life [years]	Thermal Neutron Total Cross-Section [barns]
^{152}Gd	0.2	1.08×10^{14}	1.04×10^{3}
^{154}Gd	2.2	Stable	90.9
^{155}Gd	14.8	Stable	6.09×10^{4}
^{156}Gd	20.5	Stable	6.68
^{157}Gd	15.7	Stable	2.55×10^{5}
^{158}Gd	24.8	Stable	7.84
^{160}Gd	21.9	1.30×10^{21}	10.8

Gd-157 accounts for 15.7 percent of natural Gadolinium. The isotopic composition of natural Gadolinium is listed in Table 3. Neutron capture by Gd-157 results in the meta-stable Gd-158 nucleus as described in (2) [3][4][13]. The subsequent de-excitation of this excited nucleus results in the release of gamma energy and, 19.1% of

the time, internal conversion (IC) electrons [3][9]. The de-excitation schemes of the three

most probable routes resulting in IC electrons are summarized in Figure 5.
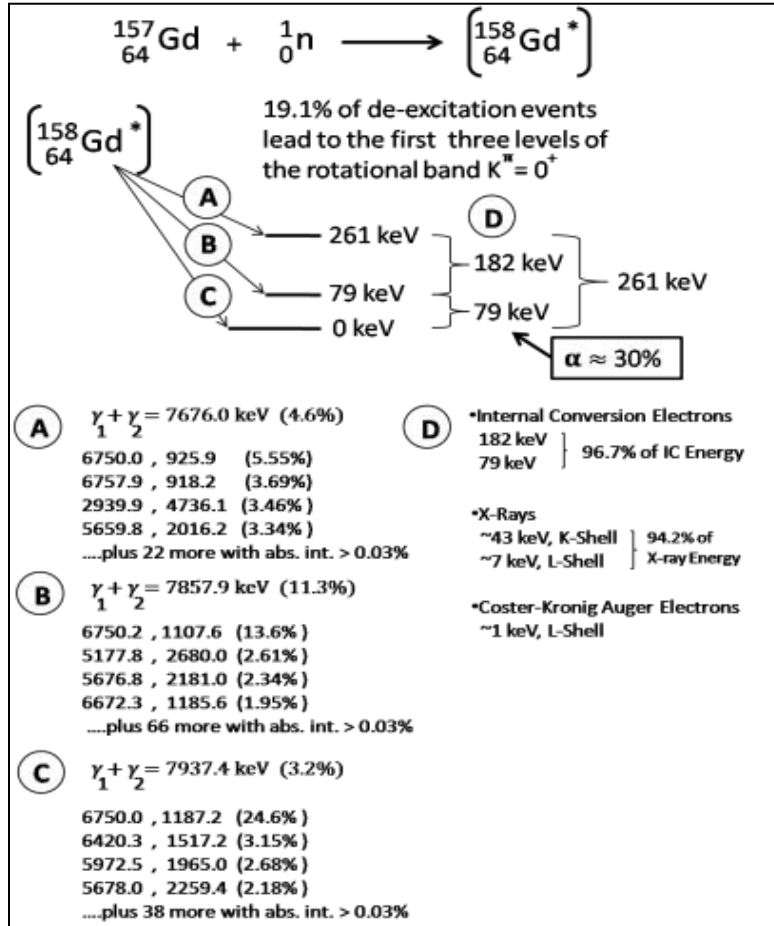
Figure 5. Summary of the schemes of the three most probable de-excitations of the excited ^{158}Gd nucleus resulting in release of internal conversion (IC) electrons. IC electrons of 79 keV and 182 keV serve as ionizing particles in the Gd_2O_3 on SiC neutron detector [3][9][13].

2.3 The p-n Heterojunction

After its discovery by Russell Ohl of Bell laboratories in 1940, the p-n junction

opened the door for the information age and serves as a key constituent of every solid-

state electronic device in use today [10]. A semiconductor material that has an excess of

acceptor dopants, typically from column III of the periodic table for a column IV

11

semiconductor, is known as a p-type semiconductor. These defects accept loosely bound electrons in the material, leaving an excess of holes which, consequently, become the majority charge carrier of the material. Conversely, an n-type material has an excess of donors that donate electrons, thereby resulting in electrons serving as the majority carrier. Neglecting the actual growth or deposition process for the moment and assuming an ideal environment, two semiconductor materials of opposite type abruptly joined together experience a re-arrangement of carriers due to drift and diffusion caused by the respective charge of the carriers and the space charge left behind when these charge carriers move.

Once thermal equilibrium is reached, there exists a region surrounding the junction of the two materials which is depleted of the majority carriers in each of the two semiconductor materials. This region is aptly named the depletion region. The width of this depletion region extends farther into the side of the less doped material due to the number of carriers available. Where the carriers have moved, space charge is left behind in each material. The difference in polarity in the space charge regions surrounding the junction forms an electric field in the depletion region. This charge distribution is represented by Poisson's equation as

$$\frac{d^2\psi}{dx^2} = -\frac{q}{\varepsilon_s}\left(N_D - N_A + p + n\right), \tag{3}$$

where ψ represents the electrostatic potential, q is the elemental charge of the electron, ε_s is the dielectric constant, and N_A and N_D are the acceptor and donor concentrations, respectively [16].
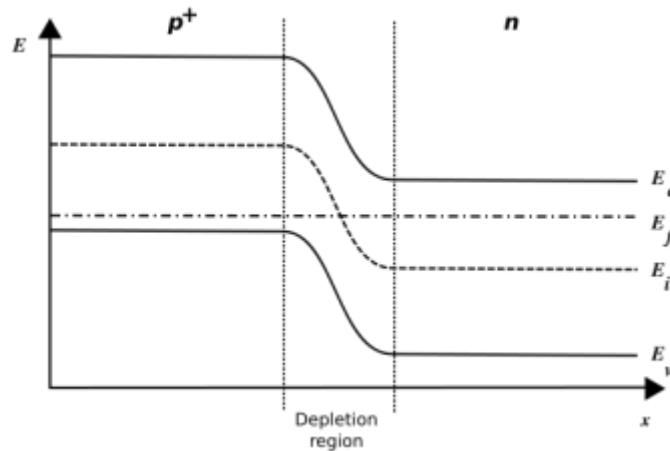
Figure 6. Energy band diagram of an abrupt p-n homojunction [11]. The Fermi level energy of each type if material must align, creating the band bending at the junction.

A p-n homojunction consists of two like semiconductor materials doped to different majority carrier concentrations. Figure 6 depicts the energy band diagram of a p-n homojunction at thermal equilibrium. The Fermi energy, E_f, represents the energy where there exists a 50 percent probability of an electron occupying that energy state. Above E_f, the probability of occupation by an electron is less than 50 percent, while below E_f, the probability is greater than 50 percent. The intrinsic Fermi energy, E_i, represents the Fermi energy of the un-doped semiconductor and generally lies very near the middle of the bandgap. The material on each side of the junction has an identical bandgap and the Fermi energy level of each type of material aligns, requiring the energy bands to bend at the junction. This band bending corresponds to the depletion region surrounding the junction. The same basic concepts apply to abrupt junctions of semiconductor materials with different bandgap energies, however, proper treatment of each material's properties must be taken into account.

13

The built-in voltage of the abrupt p-n homojunction is given by

$$V_{bi} = \frac{kT}{q} \ln\left(\frac{N_A N_D}{n_i}\right),$$ (4)

where k is the Boltzmann constant, T is the temperature in Kelvin, q is the elemental

charge of the electron, and n_i represents the intrinsic carrier density [16]. It follows from

integrating (3) for each depleted region surrounding the junction that the total depletion

width for the p-n homojunction is given by

$$W = \sqrt{\frac{2\varepsilon_s}{q}\left(\frac{N_A + N_D}{N_A N_D}\right)V_{bi}},$$ (5)

where ε_s represents the dielectric constant of the material. In the case where one side of

the junction is doped to a significantly higher concentration, (5) collapses to

$$W = \sqrt{\frac{2\varepsilon_s V_{bi}}{q N_b}}.$$ (6)

N_b in this case refers to the relatively lightly doped bulk concentration. As a bias is

applied across the p-n junction, (6) becomes

$$W = \sqrt{\frac{2\varepsilon_s \left(V_{bi} - V\right)}{q N_b}}.$$ (7)

A positive voltage applied to the p-type material corresponds to the forward bias

condition. The depletion width collapses in the forward bias condition as the applied bias

nears the built-in voltage. A negative bias applied to the p-type material puts the junction

in the reverse-bias condition. Figure 7 depicts a p-n junction in both the forward and

reverse-bias conditions.
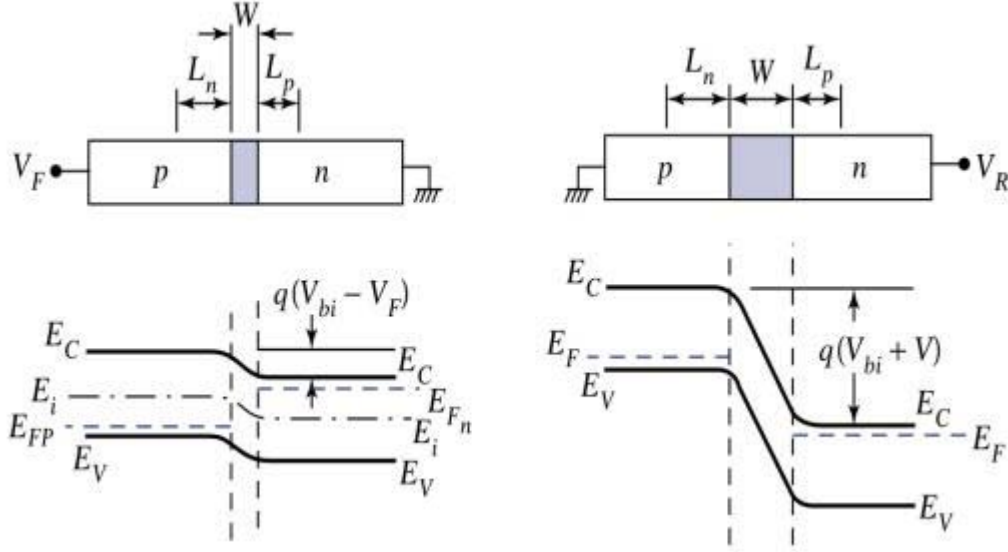
Figure 7. The energy band diagram of a p-n homojunction under bias. The diagram to the left depicts the forward bias condition. Positive bias applied to the p-type material collapses the depletion region and lowers the energy barrier, allowing current to flow more easily. The diagram to the right depicts the reverse bias condition. Positive bias applied to the n-type material increases the band bending, thus raising the energy barrier and widening the depletion region [11][12].

A p-n heterojunction consists of a junction of two dissimilar semiconductor

materials with different energy band gaps, creating an energy barrier for the charge

carriers. In the case of the heterojunction diode, the built in voltage is the sum of the two

different semiconductor materials, and is given by

$$V_{bi} = V_{b1} + V_{b2}.$$
(8)

The built-in voltages of each of the constituent materials are

$$V_{b1} = \frac{\varepsilon_2 N_2 (V_{bi} - V)}{\varepsilon_1 N_1 + \varepsilon_2 N_2}$$
(9)

15

and

$$V_{b2} = \frac{\varepsilon_1 N_1 (V_{bi} - V)}{\varepsilon_1 N_1 + \varepsilon_2 N_2}, \qquad (10)$$

where ε is the respective dielectric constant and N is the respective majority carrier concentration [16]. The depletion depth in each material is then calculated as

$$x_1 = \sqrt{\frac{2\varepsilon_1 \varepsilon_2 N_2 (V_{bi} - V)}{qN_1 (\varepsilon_1 N_1 + \varepsilon_2 N_2)}}, \qquad (11)$$

and

$$x_2 = \sqrt{\frac{2\varepsilon_1 \varepsilon_2 N_1 (V_{bi} - V)}{qN_2 (\varepsilon_1 N_1 + \varepsilon_2 N_2)}}. \qquad (12)$$

The total depletion width is, therefore, the sum of the depletion depth in each material and is given by

$$W = x_1 + x_2. \qquad (13)$$

Thus, from (11) and (12) it is clear that the depletion width is a function of the applied voltage. It is this depletion width that serves as the active region of a solid-state radiation detector. Impinging radiation deposits its energy through ionization of the constituent materials, creating e-h pairs that are swept out of the depletion width by the electric field and collected as a signal. As the depletion width increases as a function of applied reverse bias, the active volume of the detector increases.

2.4 Previous Research

While the high thermal neutron cross-section of Gd-157 and the resultant reaction products make it a natural candidate for use as a detector material, successful incorporation of a Gd based or Gd doped layer into a p-n junction has proven difficult. Previous research with Gd doped halfnium oxide (HfO_2) on n-type silicon diodes offered promising results. Pulse height spectra of the reverse biased diodes placed in a thermal neutron flux of approximately 600 n cm^{-2} s^{-1} bear a strong resemblance to a pulse height spectrum predicted by a Monte Carlo N-Particle Transport code (MCNP5.0) , as shown in Figure 8 [29].
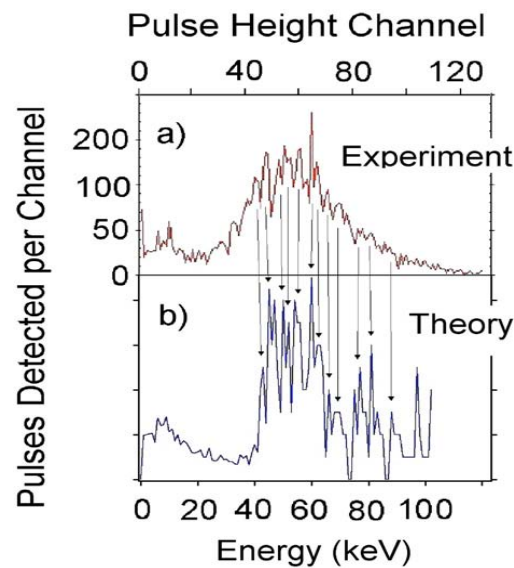
Figure 8. The pulse height spectrum of reverse-biased Gd doped HfO_2 diodes irradiated with a thermal neutron flux of approximately 600 n cm^{-2} s^{-1} compared to the spectrum predicted by an MCNP5 code. The arrows indicate energies where the predicted model agrees strongly with the experimentally obtained spectrum [29][30].

As shown in Figure 9, a plot of voltage versus time of the reverse-biased diodes irradiated with a PuBe source neutron flux of approximately 600 n cm^{-2} s^{-1} reveal pulses indicative of neutron capture and internal conversion electron emission, as well as

17

smaller amplitude pulses suggesting K-shell Auger electron resonances [29][30].

Similarly, in situ measurements taken during the irradiation of Gd doped HfO_2 on Si

diodes in the high neutron flux environment of a nuclear research reactor (approximately

10^{11} n cm^{-2} s^{-1}) showed features in the pulse height spectra purportedly resultant from the

detection of 79 keV IC electrons [30]. However, subsequent AFIT efforts to duplicate

these results have failed.
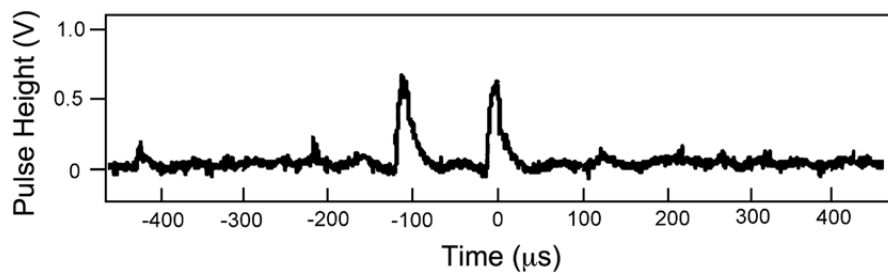
Figure 9. Pulse height train of a Gd doped HfO_2 film on n-type Si substrate diode irradiated with PuBe source neutron flux of approximately 600 n s^{-1} cm^{-2}. The two large pulses at roughly -100 μs and 0 μs are believed to correspond to the 79 keV IC electron resulting from neutron capture by a Gd-157 nucleus [29].

Neutron detection using a p-n heterojunction diode consisting of Gd_2O_3 on p-type

silicon was unable to ascertain any results conclusive of neutron interaction within his

diodes. Similar to the previous research involving Gd doped HfO_2, high leakage currents

at relatively low reverse bias voltages prevented full depletion of the diodes [3][30].

However, pulse height spectra collected from the reverse-biased Gd_2O_3 on Si diodes were

recorded in the thermal neutron environment of the AFIT Standard Graphite pile, and an

increase in recorded counts in the pulse-height spectrum with the application of a

cadmium shield was observed. Young postulated that this increase in counts was a result

of the cadmium down-scattering higher energy gamma rays present in the neutron

environment [3]. These diodes were considered blind to higher energy gamma rays due to

their relatively small size [29][30]. These down-scattered lower energy gammas had a higher probability of interaction within the detector volume, and, thus, contributed to the collected signal. He concluded that while the detector could not discriminate neutron interaction from other radiation interactions, the detector demonstrated some sensitivity to radiation.

III. EXPERIMENTAL APPROACH

3.1 Introduction

The experimental approach for this research was divided among three main thrusts: Modeling the devices, creating and characterizing the devices, and finally designing and executing the experiment. While the three thrusts were managed concurrently over the course of the research, each built upon the others. The modeling provided the insight to resolve issues encountered during device fabrication and characterization. Both of these efforts laid the foundation for the actual experiments.

3.2 Modeling the Detector

Various modeling methods were employed to provide an expectation of experimental results. The modeling process for this research effort began with establishing an understanding of the anticipated electrical signal from the detector. First, energy deposition of the internal conversion electron was explored using a Monte Carlo based radiation transport model. Finally, the device was modeled using a Poisson based device transport code, Davinci, subjected to charge carrier deposition to understand the charge collection process.

The first step in laying the foundation for the modeling entailed understanding the depletion width created in the junction under a reverse bias. Applying the parameters of Table 4 to (11) through (13), Figure 10 shows an applied voltage of -5 V yields a depletion width of approximately 2.9 microns in the SiC based diodes. Electron-hole (e-h) pairs created outside of the depletion width by ionizing particles have a material dependent lifetime. Within the span of this lifetime, the electrons will drift for a distance

known as the diffusion length before recombination. The e-h pairs are created within one

diffusion length of the depletion region, therefore, have a probability of diffusing into the

depletion region.
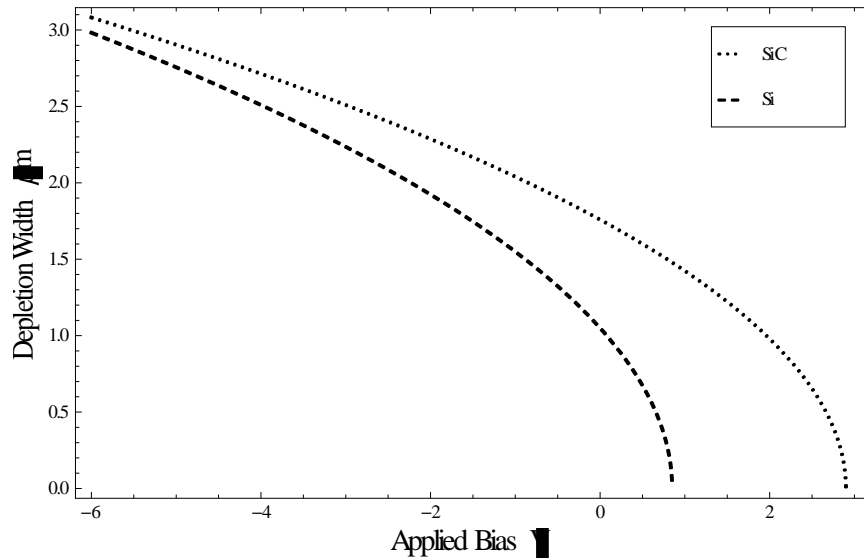
Figure 10. Depletion width plotted as a function of applied bias. Using the material characteristics from Table 4, a reverse bias voltage of 5 V yields a depletion width of approximately 2.9 microns in the SiC based diode and 2.7 microns in the Si based diode. An applied reverse bias of 2500 V creates a depletion width of approximately 56.9 and 51.7 microns in the SiC and Si diodes, respectively. The goal of achieving the greatest possible depletion width is offset by the reverse bias leakage current.

The SiC substrate for the samples prepared for this experiment is the 4H polytype

with an electron diffusion length of approximately 1.5 microns [17]. Thus, the effective

collection width with a reverse bias voltage of 5 V is approximately 4.4 microns. With a

contact diameter of 1mm, this collection width yields an active detector volume of

approximately 3.46×10^{-6} cm^3.

Table 4. Semiconductor Material Parameters used to model the Si and SiC based diodes[3][14][16][22][23][24].

Parameter	p-type Si	p-type SiC	n-type Gd$_2$O$_3$	Units
E$_g$	1.12	3.2	3.8	eV
χ	4.05	3.5		eV
N$_A$	10^{15}	10^{15}		cm^{-3}
N$_D$			1×10^{19}	cm^{-3}
N$_C$	2.86×10^{19}	1.69×10^{19}		cm^{-3}
N$_V$	2.66×10^{19}	2.52×10^{19}		cm^{-3}
n$_i$	9.65×10^{9}	1×10^{-7}		cm^{-3}
ε_s	11.9	9.7	17	
E$_{ion}$	3.4	9.6	11.4	eV
μ (e/h)	1450/505	720/40		cm^2/V·s

3.2a Anticipated Signal

The electric signal resulting from energy deposition does not begin when the

charge is collected on the electrode. The signal is a result of the motion of the charge

carriers. As soon as the e-h pairs are created within the depletion region, the current

begins to rise. The rise time corresponds to the time it takes to collect both electrons and

holes. Therefore, if the energy deposition is assumed at a single point, the location of the

deposition relative to the junction will determine the shape of the pulse. Assuming full

deposition of a single *IC* electron, the amount of charge created is given by

$$Q = q_e \frac{E_{IC}}{E_{Ion}},$$ (14)

where q_e is the elemental charge of an electron, E_{IC} is the energy of the *IC* electron, and

E_{Ion} is the amount of energy required to ionize an atom in the detector, or create an e-h

pair for a solid state detector0. Therefore, a 79 keV *IC* electron deposited in the SiC

portion of the depletion region $\left(E_{IC} = 9.6\,eV\right)$ corresponds to a charge deposition of

$1.318 \times 10^{-15}\,C$.

From Table 4, SiC has an electron mobility, μ, of 720 cm^2 /V s. Assuming an electric field of approximately 10^5 V/cm, the ionized electrons diffuse through the depletion region at roughly 7.2 x 10^7 cm/s. At this velocity, the time for electrons to travel across an effective collection width of 4.4μm is approximately 6.11 ps. Dividing the total charge created by full deposition of the *IC* electron by this travel time equates to a current pulse of 0.216 mA or 216 μA. While these calculations assume ideal conditions of charge deposition and neglect recombination of charge carriers, a current pulse on the order of 100's of microamps should be detectable above the leakage current of the reverse-biased diode.

While the current may be detectable above the diode leakage current, the frequency with which the signal is created and the efficiency of the collection system impact the ability to discriminate a neutron induced signal from system generated or environmental noise. The ideal frequency of the anticipated electronic signal, f_{AES}, is given by

$$f_{AES} = \frac{2\pi}{4\pi} \cdot RRD \cdot Vol_{ACL} \cdot \gamma_{Branch} \cdot \alpha \,, \tag{15}$$

where *RRD* is the Reaction Rate Density, Vol_{ACL} is the volume of the depleted conversion layer, γ_{Branch} is the probability that a nuclear reaction will result in the corresponding de-excitation, and α is the internal conversion co-efficient [3]. The

factor of $\dfrac{2\pi}{4\pi}$ is included due to the planar geometry of the device. IC electrons emitted

from the Gd$_2$O$_3$ layer have a roughly 50 percent probability of traveling toward the

substrate and, thus, the depletion region. The reaction rate density is the product of the

macroscopic cross-section, Σ, and the thermal neutron flux, ϕ, and is written as

$$RRD = \Sigma \phi. \tag{16}$$

The macroscopic cross-section is given by

$$\Sigma = \sigma N, \tag{17}$$

where σ is the microscopic cross-section, and N represents the concentration of Gd

nuclei in the conversion layer. N was calculated using (18) and the values of density,

$\rho_{Gd_2O_3}$, and molecular weight, $MW_{Gd_2O_3}$ from Table 5.

$$N = \frac{\rho_{Gd_2O_3} N_{AV}}{MW_{Gd_2O_3}} \tag{18}$$

The portion of the active detector volume that lies in the conversion layer, Vol_{ACL}, was

estimated to be that portion of the conversion layer that resides under the 1 mm diameter

contact.

Table 5. Physical Constants and parameters used to calculate the Anticipated Electric Signal Frequency [2][3][4][8].

Parameter	Value	Units
σ	46000	b
$\rho_{Gd_2O_3}$	7.41	g/cm^3
$MW_{Gd_2O_3}$	352	g/mol
N_{AV}	6.023×10^{23}	mol^{-1}
Vol_{ACL}	7.854×10^{-8}	cm^3
γ_{Branch}	11.3	%
α	30	%

Assuming a thermal neutron flux consistent with the AFIT Standard Subcritical Graphite Pile (approximately 10^4 n cm^{-2} s^{-1} in drawer 3) and applying the parameters and constants of Table5 to (15) through (18) yields an ideal anticipated electric signal frequency of 7.76 x 10^{-3} 79 keV *IC* electrons per second. This frequency is linearly dependent on the thermal neutron flux, as shown in (15). Thus, in higher flux environments such as the thermal column of a research reactor (approximately 10^{11} n cm^{-2} s^{-1}), this frequency can be adjusted to be as high as 10^5 79 keV *IC* electrons per second.

3.2b Energy Deposition Model

Given an effective detection thickness of 4.4 μm in the silicon carbide based diode reverse-biased to 5 V, a Monte Carlo simulation of electron trajectory in solids

(CASINO) was performed to determine if the conversion electrons emitted from the

Gd*-158 de-excitation could fully deposit their energy in the depletion width [18].

Figure 11 depicts the track of the simulated electrons through the silicon carbide and the

energy deposition. While a few of the electrons could conceivably deposit all of their

energy within the depletion region, the vast majority of the electrons will simply pass

through the depletion width with a probability of ionizing atoms as they transit. The

depth of penetration of the simulated electrons is depicted in Figure 12.
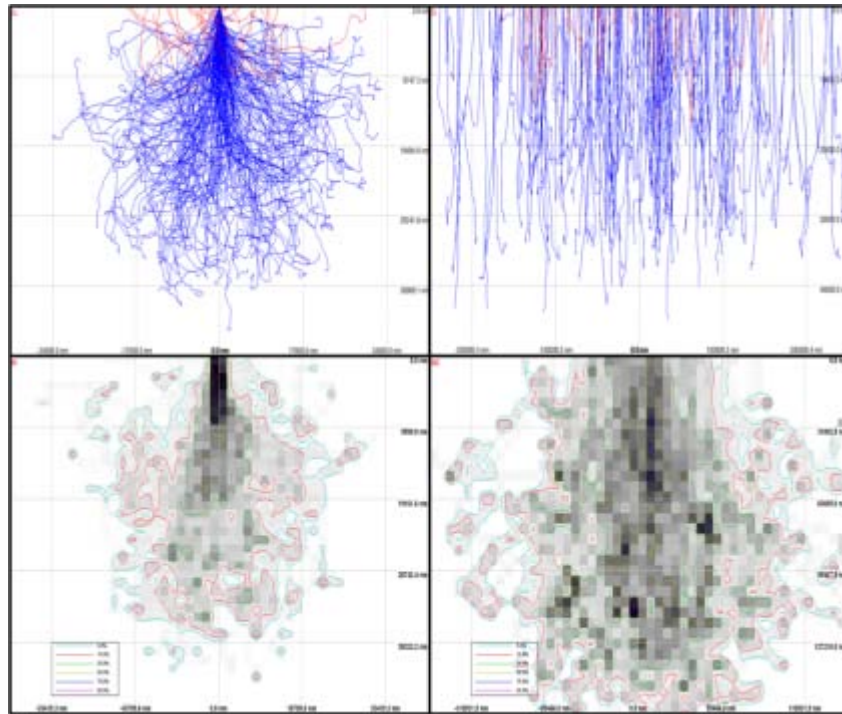
Figure 11. Results from a CASINO simulation of 10^5 79 keV electrons incident on the Gd_2O_3 on SiC diode. The plots at the top of the figure represent the track of the inbound electrons. The plots below represent energy deposition of the electrons. The plots on the left side of the figure are the results of a simulated beam of electrons, while the right hand plots resulted from a simulated planar flux of electrons.

Additionally, due to the planar geometry of the device, approximately half of the

gammas emitted coincidentally with the *IC* electrons will deposit some if not all of their

energy in the depletion region, contributing to the overall system noise. The goal is for a

substantial portion of generated IC electrons to deposit their full energy in the depletion width creating a discernable signal above this noise and any generated in the electronic signal collection equipment.
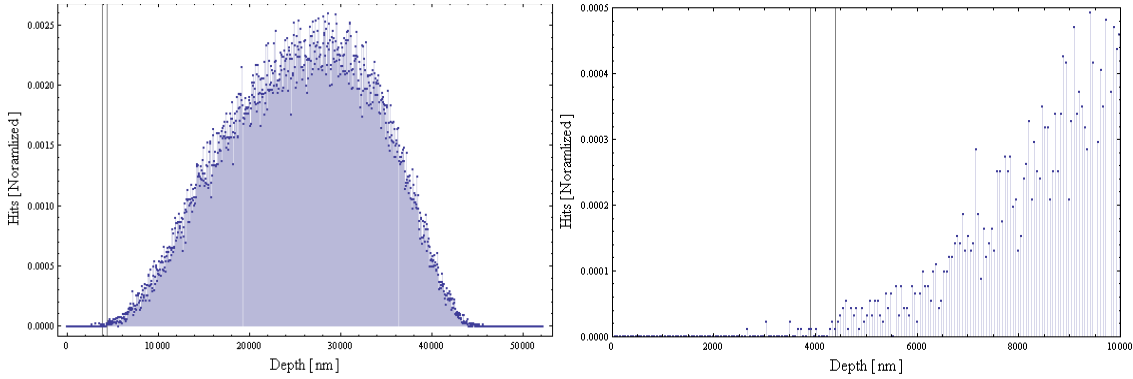
Figure 12. Depth of penetration of the 79 keV electrons. The left plot represents the entire distribution of complete deposition ranging from approximately 2-480 microns. The right plot is an enlargement of the lower end of the distribution. The area to the left of the left vertical line in each figure represents the depletion region and the area between the vertical lines represents the diffusion length of electrons in SiC. Approximately 0.02 percent of the 10^5 incident electrons fully deposited their energy within the depletion region plus one diffusion length.

Analysis of the data from the 10^5 electron CASINO simulation shows that 0.021% of the 79 keV electrons are completely absorbed in the depletion region, while 0.00001% of the 182 keV electrons are completely absorbed. Those electrons that do not deposit their entire energy within the depletion region will still ionize atoms and deposit a portion of their energy along their track through the material. Those e-h pairs created within the depletion region and a portion of those created within one diffusion length of the depletion region will contribute to the signal created by the detector.

3.2c Diode Modeling

Davinci software was employed to model the diode characteristics of both the Gd_2O_3 on Si and Gd_2O_3 on SiC samples. Davinci is a 3D semiconductor modeling

27

program that solves for the carrier concentration and current using Poisson's equation and the current continuity equations over a nodal grid. This allows for simulation of various common semiconductor materials in an unlimited number of configurations. For an accurate depiction of the Gd_2O_3 conversion layer, a generic semiconductor material was modified with the parameters listed in Table 4. The number of available simulation nodes precluded simulation of a full scale device. Therefore, a 3D column, the cross-sectional area of which represents a pixel of the contact surface, served as the diode model as illustrated in Figure 13.
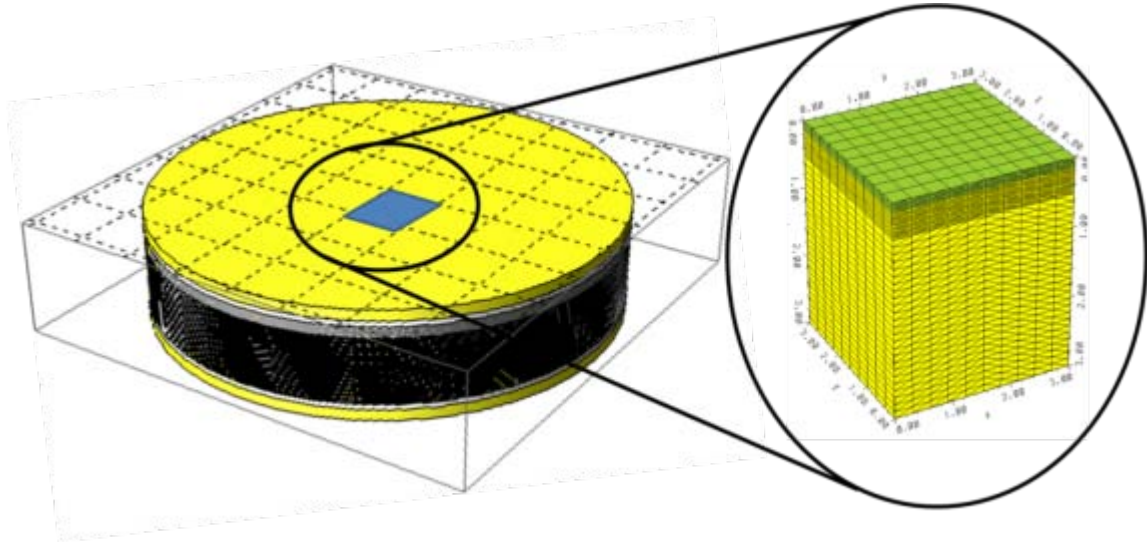
Figure 13. A plot of the model geometry is shown at the right. The Davinci model's rectangular geometry effectively serves as a pixel of the face of the actual diode. The relatively large surface area of the actual diode required the scaling of the Davinci model to allow enough nodes for the program to converge on a solution.

The total current through the device, $\vec{I}$, is given by

$$\vec{I} = \vec{J} \cdot A,$$ (1.19)

where $\vec{J}$ is the current density in A/cm^2, and A represents the cross-sectional area of the device in cm^2. Thus, the current density is given by

28

$$\vec{J} = \frac{\vec{I}}{A}. \tag{1.20}$$

Applying the values listed in Table 4 to the semiconductor parameters in the code

(Appendix C), the Davinci model predicts a leakage current on the order of 10's of pA at

a reverse bias of 1.5 V. The area of the modeled column is 9 μm^2. The cross-sectional

area of the actual diode is given by

$$A = \pi \cdot r^2, \tag{1.21}$$

where r is the radius of the contact. With a diameter of approximately 1 mm, the diode

has an assumed calculated cross-sectional area of approximately 7.9 x 10^5 μm^2. Thus the

current predicted by the Davinci model must be scaled by a factor of 3.5 x 10^5 to

accurately reflect the true device dimensions. The scaled I-V results of the Davinci model

plotted with measured values from sample Y3 are shown in Figure 14.
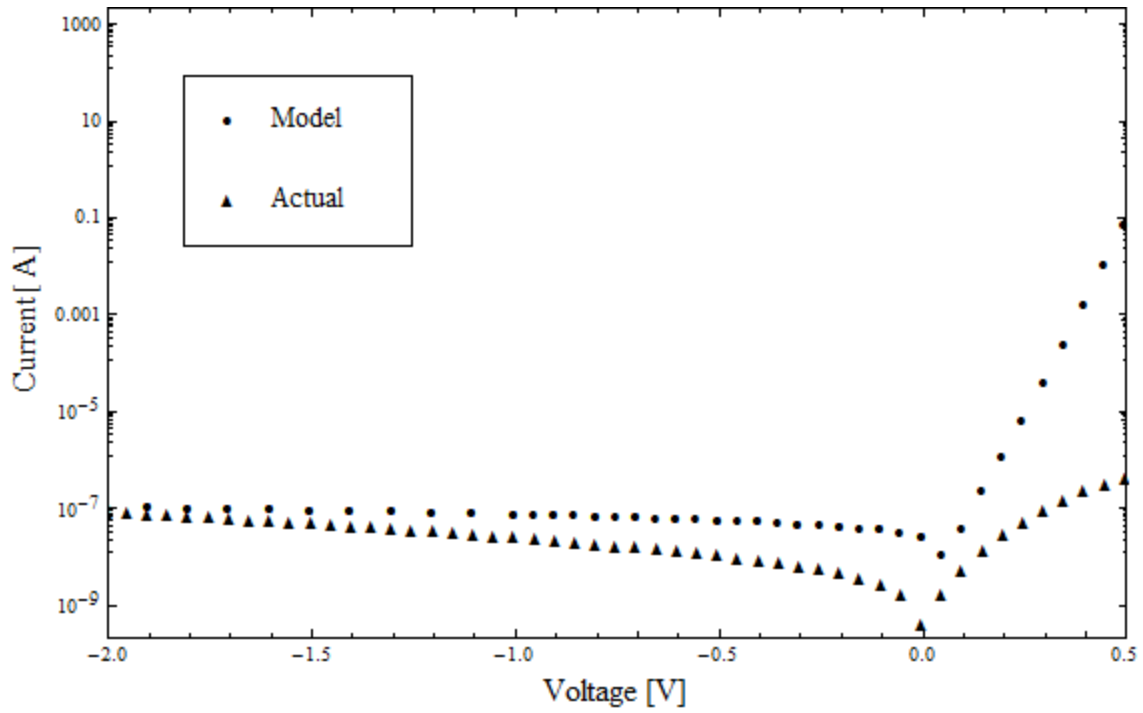
Figure 14. The Davinci model I-V response versus an actual measurement from sample Y3. A generic semiconductor with modified parameters was used to simulate the Gd_2O_3 layer.

Once the Gd_2O_3 parameters were set, the PHOTOGEN command was used to simulate the generation of e-h pairs by an energetic charged particle. The PHOTOGEN statement allows the injection of a charged particle by reading in a linear energy transfer (LET) file and applying that transfer of energy to a user specified generation track. The various LET files used in the modeling are shown in Table 6.

Table 6. Linear energy transfer data. The data listed below is contained in a data file read by the PHOTOGEN statement in the Davinci ionization model [8][25].

Depth	79 keV ICe	182 keV ICe	Heavy Ion
[µm]	[pC/µm]	[pC/µm]	[pC/µm]
0	3.93511E-05	2.43148E-05	0.17
1	3.96411E-05	2.43459E-05	0.17231
2	3.99621E-05	2.43873E-05	0.17444
3	4.0252E-05	2.44184E-05	0.17639
4	4.05627E-05	2.44495E-05	0.17816
5	4.08941E-05	2.44909E-05	0.17975
6	4.12255E-05	2.45427E-05	0.18116

The current and voltage are profiled during charge generation and collection at 5 ps intervals. The current as a function of time is plotted as well as the current integrated over time as depicted in Figure 15. Additionally, the contact voltage is plotted as a function of time. The results shown in Figure 15 correspond to the heavy ion LET file shown in Table 6. No current was produced during the Davinci simulations using the electron LET data files.. This is believed to be due to the low probability of interaction of electrons of these energies in such a short distance. The linear energy transfer of the electron increases as it slows down. Unfortunately, the maximum track distance for the 79 keV electron in this model is 5.2 µm, which does not allow for much energy transfer and generation of a statistically significant number of charge carriers.
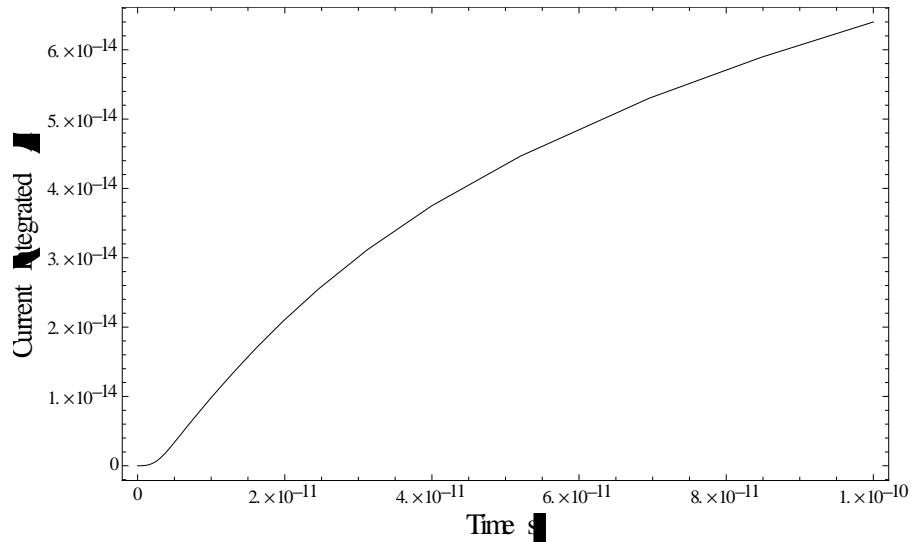
Figure 15. The integrated current measured on the contact of the diode over 100 picoseonds for a 100 MeV Argon ion.

The heavy ion model, however, generates an integrated current of roughly 64 fA over 100 ps, corresponding to a current pulse of 0.64 mA. While this is three times larger than the pulse predicted by (14), the ion transferred more than 79 keV of energy in its 5.2 μm path.

The final output of the model is a contour plot of the electron and hole currents during the PHOTOGEN measurements. The various insets in Figure 16 illustrate the hole concentration in the diode during and after the ion deposits energy along its track through the volume. The different contours shown in the figure represent a change in hole concentration by a factor of 100. The ion entered the model in the top from corner and exited through the bottom back corner. The intervals shown are 1 , 3.4, 17, and 100 picoseconds.

32
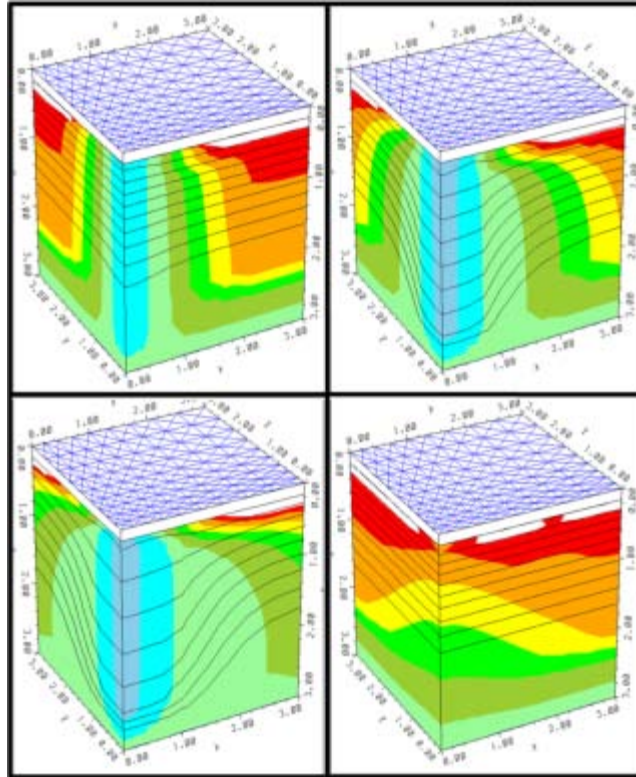
Figure 16. The hole current from the heavy ion model at various times during charge collection. The times, from left to right, top to bottom, are 1 ps, 3.4 ps, 17 ps, and 100 ps, respectively. The contours represent a change in the hole concentration by a factor of 100. The white areas surrounding the top contact represent a hole concentration of less than 10^4cm^{-3} [25].

3.3 Diode Fabrication and Characterization

Device construction began with samples consisting of a substrate material with a thin layer of Gd_2O_3 on one surface. The Si based samples were prepared and contacts deposited in 2009. The samples had been previously studied, and signs of damage to the contact and surface were visible. Figure 17 shows the damage to the surface and stress induced damage to the edge of one sample as imaged by the scanning electron microscope (SEM).
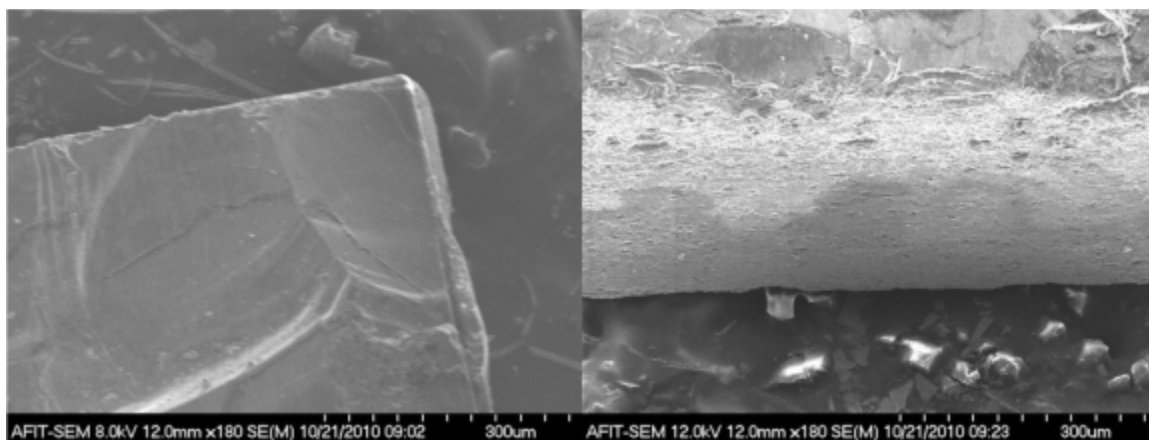
Figure 17. Two different edges of a Gd$_2$O$_3$ on Si sample taken with the scanning electron microscope (SEM). Notice the damage due to stress.

During previous research efforts using the Si samples, a degradation of the diode characteristics was observed over time. In contrast to the stress evident on the Si samples, Figure 18 shows the edges and surfaces of one of the SiC samples prepared in the summer of 2010. The amorphous nature of the SiC substrate is clearly visible.
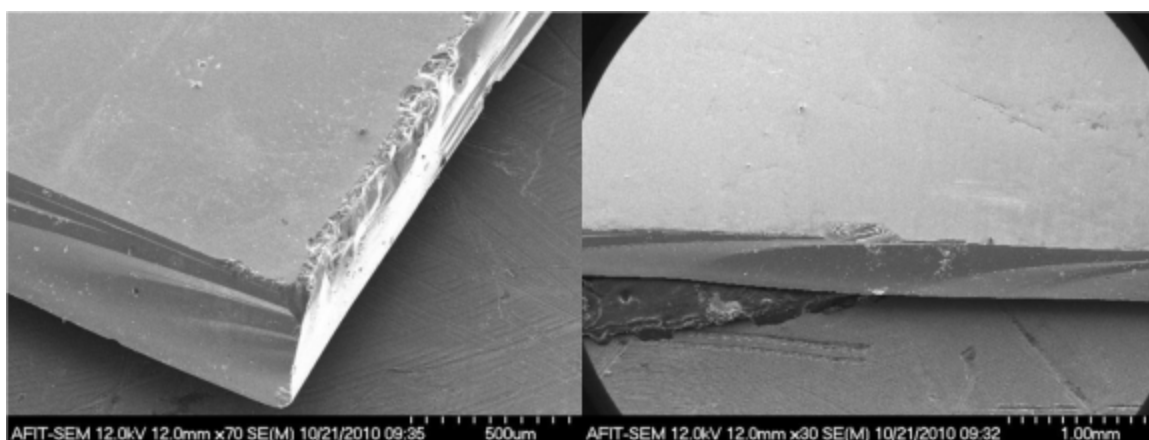
Figure 18. Gd$_2$O$_3$ on SiC samples. Notice the striations due to the amorphous nature of the substrate. While chipping is visible on the edges, the overall integrity of the sample appears intact.

3.3a Fabrication

The silicon-based samples used in this experiment consisted of Gd_2O_3 deposited on p-type Silicon (Si) in a critical water deposition reactor. Gold contacts were then sputtered onto the surface of the Gd_2O_3 in a five contact by five contact grid, while a roughly 1 cm^2 square gold contact was sputtered onto the reverse side of the sample to serve as a common contact. Significant changes in the diode behavior of the samples were believed to have occurred in the span of less than two months from construction and initial characterization to delivery of the samples. Many of the samples failed to rectify, while the remainder experienced significant leakage current under reverse bias.

This perceived degradation of diode behavior was thought to be due to a reaction resulting from the differences in surface chemistry between the deposited thin film and the substrate. Thus, a substrate of SiC was chosen for the samples created for use in this experiment to mitigate the degradation of the diode. The SiC substrate samples were prepared via pulsed laser deposition (PLD), whereby a target material under high vacuum is vaporized by a high energy laser. The substrate wafer faces the target and the vapor deposits on the surface as illustrated in Figure 19. For these diodes a target of pure Gd_2O_3 under a vacuum of 10^{-5} Torr was used in fabrication. The deposition occurred under a flow of H_2, ensuring the necessary oxygen vacancies to render the film semiconducting 0. Layer deposition on the SiC substrate was confirmed by x-ray diffraction (XRD), however, no ellipsometry or other characterization measurements were taken. The samples were then shipped to AFIT for contact application and experimentation.
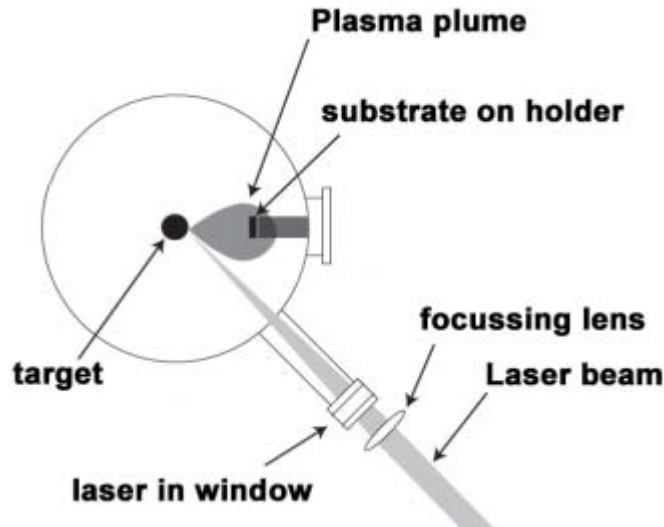
Figure 19. Simplified depiction of the orientation of the substrate and target during pulsed laser deposition. The target is vaporized by a high energy laser beam. The vapor then deposits on the substrate, the desired surface facing the target in situated in the vapor cloud [15].

Three separate SiC samples, each approximately 1 cm^2, were provided. Two samples were prepared under an H_2 flow, and one without the H_2 flow. One of the two samples prepared under the H_2 flow was cut to make five separate samples, while the remaining two samples were left intact. Contacts were applied to all of the samples prepared under H_2 flow using two different recipes. The sample left intact had a single contact approximately one quarter of an inch in diameter applied to both surfaces. A Keithley 4200 Semiconductor Measurement System (SMS) connected to a Signatone Model CM-220 probe station was employed to take initial C-V measurements to verify diode rectification.

The intact sample failed to exhibit any diode-like behavior. The remaining samples prepared under H_2 flow had multiple contacts using different contact metal recipes applied to the Gd_2O_3 layer and common contacts applied to the substrate surfaces. A total of 16 contacts were applied among the five samples. Only one contact on sample

36

T5 exhibited any diode-like behavior. The sample rectified, however, the leakage current at a reverse bias of 1.5 V was measured to be approximately 10 µA, more than an order of magnitude greater than leakage currents achievable with the Si based samples.

In order to maximize the number of samples and allow for multiple diode packaging configurations, the SiC based samples and all but two of the remaining Si based samples were cut down to smaller size. The samples were placed with the Gd_2O_3 layer facing down on a Micro Automation Model 140 mounting station inside a 4 in. stainless steel frame. Blue high tack tape was then pulled over the frame and pressed with a handheld roller. The excess tack tape was trimmed off and the frame removed from the mounting station. The frame was then placed tack tape side down on a Semiconductor Equipment Corp. Model 2650 Die Matrix Expander. The frame and tape were heated to 75° C for approximately 5 minutes to ensure adhesion of the sample to the tack tape. The sample and tack tape were then measured with a Bausch and Lomb DR 25B optical gauge. The frame was then loaded and affixed onto the articulated table of a Micro Ace Loadpoint Limited computer controlled saw.

Figure 20. The uncut samples were placed on the Micro Automation Model 140 mounting station (top left) and pressed with high tack tape. The frame and tape with the sample attached was then heated on the Die Matrix Expander (bottom left). Once the tape had heated sufficiently to securely adhere the sample, the frame was loaded onto the Micro Ace saw (right).

After inputting the thickness obtained from the optical gauge, the saw performed a blade depth calibration routine. Alignment of the sample was accomplished with the aid of an integrated camera. A stationary diamond coated 0.0012 inch rotary saw blade cooled in a stream of tap water then cut the sample moving on the computer controlled table. Once each cutting pass was complete, the next cutting pass was input into the computer. This saw allows easy cutting of precise angles even with smaller samples. Care was taken to ensure that the samples adhere to the tack tape since the cooling stream of water was provided at a pressure of 10 to 15 psi. Samples that do not properly adhere to the tape tend to dislodge under the pressure of the coolant and must be retrieved from the coolant drain filter. If this filter is not cleaned regularly, it can prove difficult to determine which fragment caught in the filter is the dislodged sample. One such sample had to be discarded because its identity could not be determined with certainty.

38

Figure 21. The Electron Beam Evaporator in the AFIT Clean Room used to deposit contacts on the samples is shown in the left of the figure. Samples were fastened to the the mask and loaded into the spindle (top middle), which was then secured in the evaporator chamber (top right). The hearth in the floor of the chamber (bottom right) can accommodate up to five crucibles (bottom middle) loaded with a target metal.

Contacts were next applied to the samples using three different facilities and four different recipes. Table 7 lists the contact recipes for the samples used in this experiment. Prior to contact application, the samples were cleaned in an ultrasonic cleaner with five minutes in acetone followed by five minutes in methanol.

Table 7. The different recipes used for contact application are listed below. Different recipes were explored in an effort to create an ohmic contact, as well as to create contacts that could accommodate the ultrasonic wire bonding process used in the 16 pin chip packages assembled by AFRL.

AFIT Clean Room		AFRL Sensors Directorate	
Recipe 1*	Recipe 2	Recipe 3	Recipe 4
150 Å Al	200 Å Ti	200 Å Ti	200 Å Ti
500 Å Au	2000 Å Au	2800 Å Au	1000 Å Au

*UNL personnel used this recipe for contact deposition on the set of samples with a silicon substrate study by C. Young in 2009 [3].

After a final five minutes in isopropyl, the samples were placed in a pressurized flow of N_2 to dry and remove any remaining precipitates. The cleaned samples were then placed in a contact mask and affixed into a spindle. The spindle was bolted into the ceiling of the Torr International E-Beam Evaporator. The target metals were placed in 1 in. diameter crucibles and then loaded into the hearth of the E-Beam Evaporator. The hearth can accommodate up to five different metals. The chamber was then sealed and evacuated in a two-stage process to a pressure of approximately 5×10^{-6} Torr. Once high vacuum was achieved, an electron beam was trained onto the target metal which then vaporized. The vapor then rose to the ceiling of the chamber and coated the samples turning in the spindle at a rate of approximately 2-3 Angstroms per second as measured by a quartz sensor. Figure 22 provides a depiction of the typical contact orientation and device architecture.
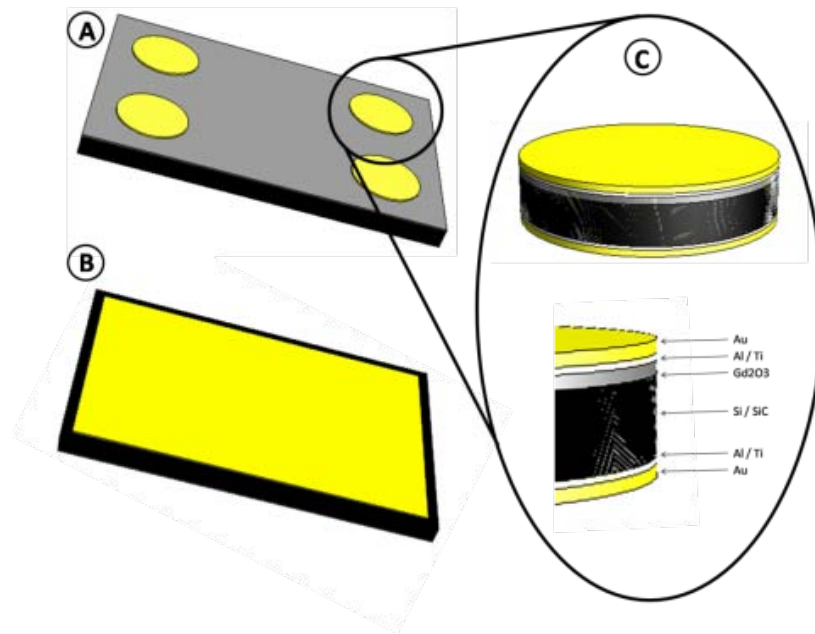
Figure 22. Typical contact orientation and intended diode architecture. (A) shows the arrangement of the contacts as dictated by the hole spacing on the available mask. The common substrate contact is shown in (B). (C) depicts the intended architecture and the contact seed layer, deposited to ensure an ohmic contact.

40

After contact application, the samples were mounted in a variety of packages. Initially, the samples were levitated to isolate them from any other material and provide access to the contacts for wire bonding. The sample holders proved difficult to manipulate without stressing the wire bonds. This method was abandoned in favor of gold and Lexan polycarbonate packages. Examples of the various sample packages are shown in Figure 23.
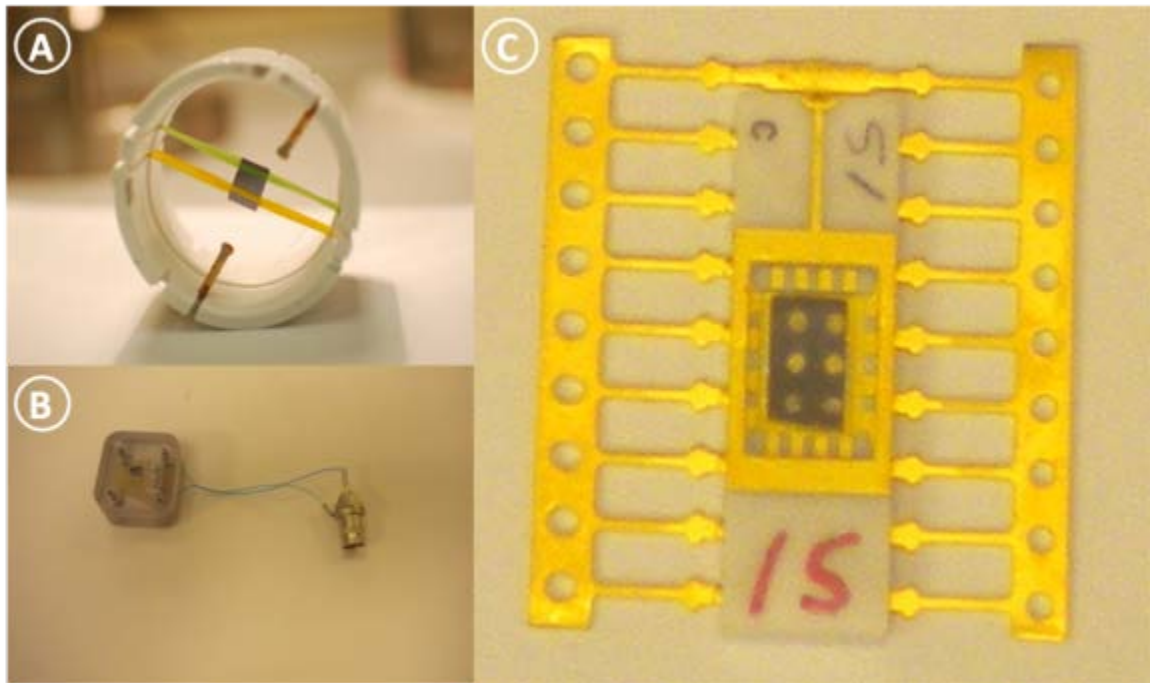
Figure 23. The various packaging methods devised for the diodes. Initially the diodes were levitated and gold wire was painted on to the contacts and two conducting posts as shown in (A). The diodes were then placed in Lexan boxes with gold wire painted onto the contacts and posts (B). Wires were soldered to the conducting posts and BNC connectors. The 16 pin diode packages shown in (C) were thought to have the most potential, however, the correct contact recipe was never attained to allow the gold wire to bond using the ultrasonic process.

The Lexan packages consist of two matching halves secured with machined screws with a cavity for the samples and two conducting posts. The samples sit in the cavity and are held in place by thin gold wire connecting the contacts to the conducting posts. The gold wire is thin, but thick enough so that the mass of the sample will

permanently bend it. The wire is painted onto the contacts with a silver-doped paint. The silver paint bonding required much iteration to achieve proficiency.

The 16 pin diode packages shown in Figure 23 were provided by AFRL. The substrate common contact was affixed to the ground contact with silver epoxy and cured in a kiln for approximately two hours. The contacts were then ultrasonically bonded to the adjacent pin leads using 0.007 inch gold wire. The gold layer on the contacts deposited with recipes 1, 2, and 4 proved too thin and the wire would not bond. Those contacts applied with recipe 3 did bond with the wire; however, it is believed that the bonding needle punched through the contact, degrading the electrical connection. While all of the various diode packaging methods worked to some degree, characterization of the diodes led to the choice of the Lexan box packages for the final device configuration.

3.3b Characterization

Subsequent to contact application and packaging, current-voltage (I-V) measurements were taken to characterize the reverse bias leakage current. The I-V characteristics of samples T5 and Y3 are shown in Figure 25. I-V measurements taken with the probe station provided good diode response; however, initial I-V measurements of packaged and bonded samples yielded leakage currents on the order of mA at corresponding reverse bias voltages of 2 to 5 V. As the silver paint bonding technique became more refined, so did the diode response. Care was taken to ensure that the silver paint remained on the contact surface and did not spill over onto the sample surface. Many of the contacts on the Si samples remaining from the UNL deposition showed signs of significant damage as depicted in Detail A of Figure 24. With as little silver-doped

42

paint used as possible, the strength of the bond began to prove problematic. Many bonds

were created and characterized only to have the bonds break after slight stress.
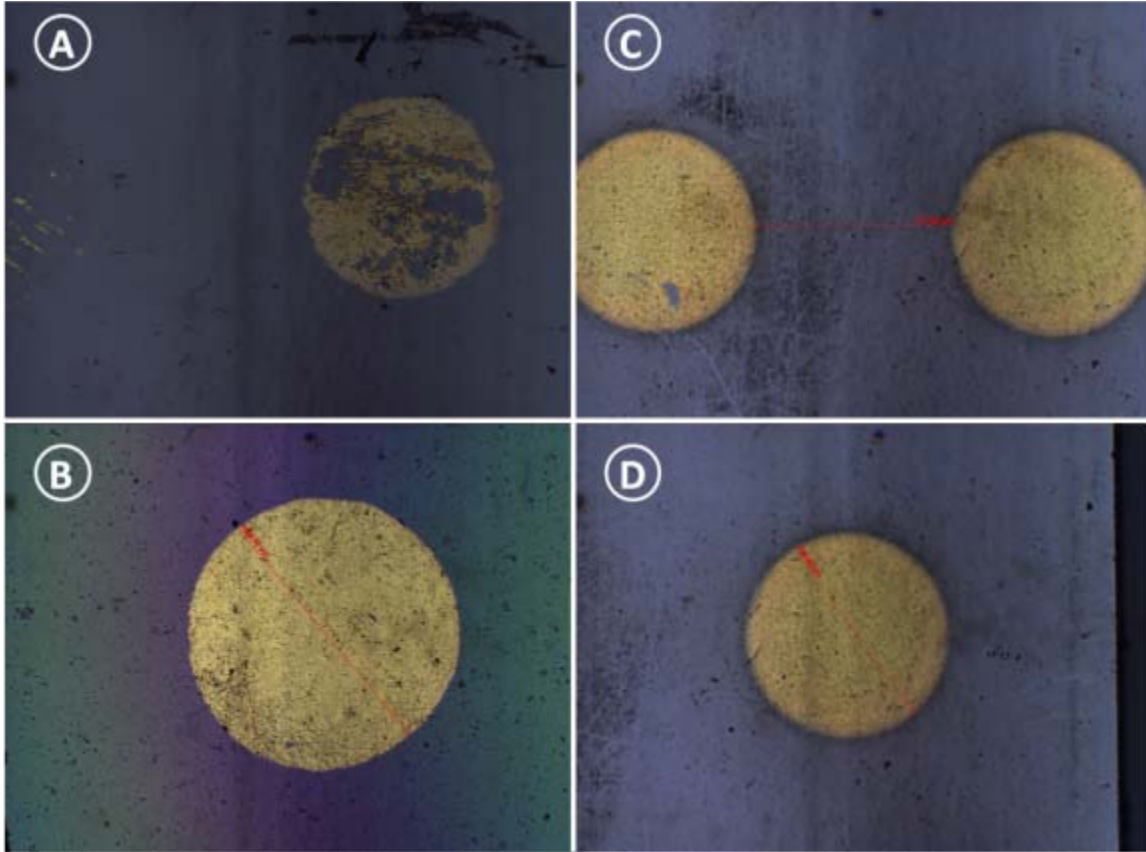
Figure 24. Contacts deposited using various recipes are shown above. The contacts shown in (A) were applied by UNL personnel using recipe 1. In the left side of (A) one can see a contact that has been nearly entirely removed. (B) shows a 1000 micron diameter contact applied using recipe 3 by AFRL. Contacts applied using recipe 4 are approximately 800 microns in diameter (D) and separated by that distance as shown in (C).

While many of the Si based samples exhibit good diode characteristics, only one

of the 16 available contacts among all of the SiC samples exhibited any diode-like

behavior when measured with the probe station. It is unclear if there was a disparity in

the deposited layer or the contact application. Sample T5 had four contacts deposited on

its surface. The only visible difference between the three contacts that did not pass

current and the one rectifying contact is a score mark on the substrate. It is possible that

an inconsistency in the layer allows current to pass in only this one location. The I-V

responses of samples Y3 and T5 are shown in Figure 25.
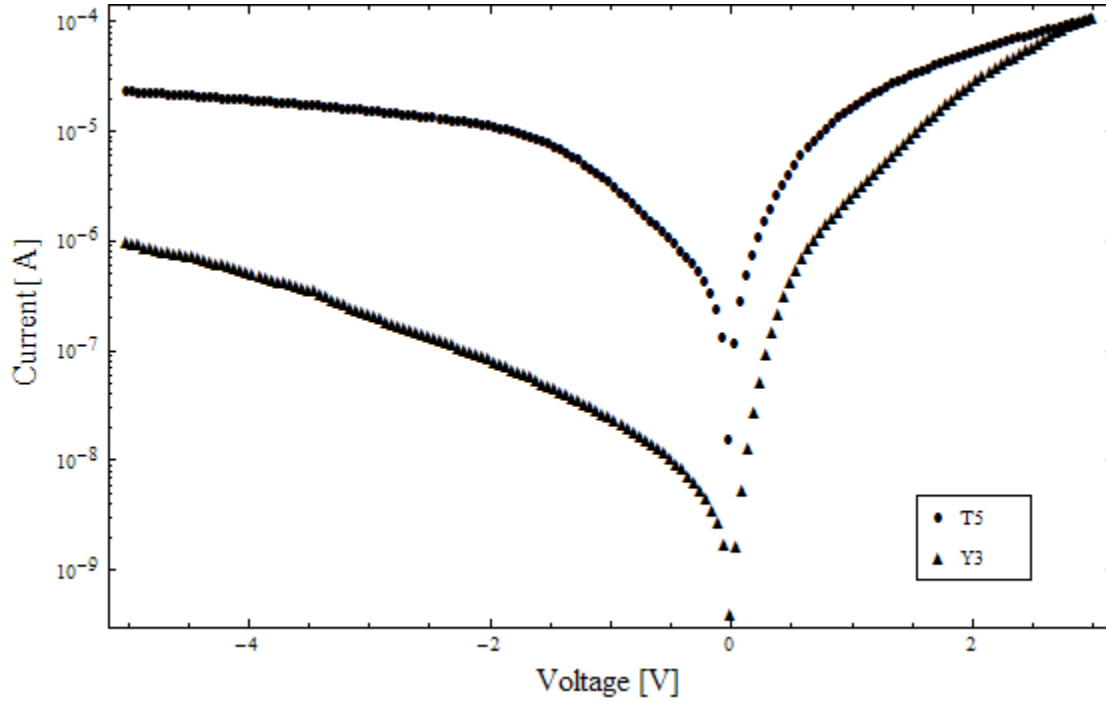
Figure 25. Final I-V Characterization measurements taken of samples T5 and Y3. Sample T5 contains the only contact among the 16 available SiC based devices that rectifies.

Capacitance- voltage (C-V) measurements were taken to determine built-in

voltages and carrier concentrations. The built-in voltage and carrier concentrations

subsequently allowed for a realistic prediction of the depletion width in the diode for

various applied voltages. The C-V response and the plot of $1/C^2$ are given in Figure 26.
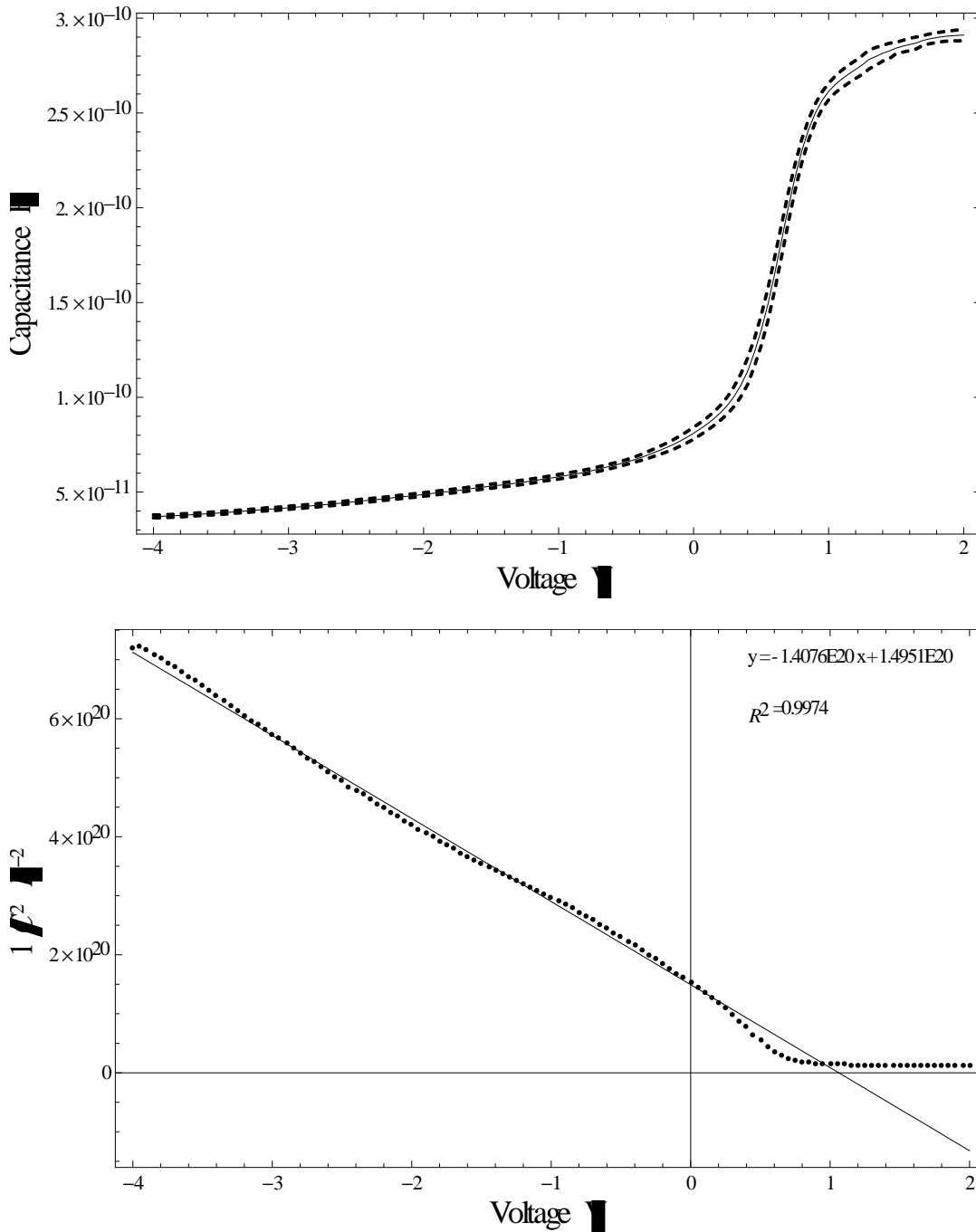
Figure 26. C-V and $1/C^2$ plots for sample Y3. The slope of the linear portion of $1/C^2$ gives the carrier concentration while the x-intercept gives the built-in voltage. The built-in voltage for this sample is estimated to be approximately 1.1 V.

From (7) for a one-sided abrupt junction, the junction capacitance, C_j, is given in units of [F/cm] by

$$C_j = \frac{\varepsilon_s}{W} = \sqrt{\frac{q\varepsilon_s N_B}{2(V_{bi} - V)}}. \tag{22}$$

The depletion width, W, can then easily be extracted from the measured capacitance as

$$W = \frac{\varepsilon_s A}{C_j}, \tag{23}$$

where A represents the area of the junction [16][21]. The depletion width taken from the C-V data obtained from sample Y3 is plotted with the value calculated from (13) is depicted in Figure 27.
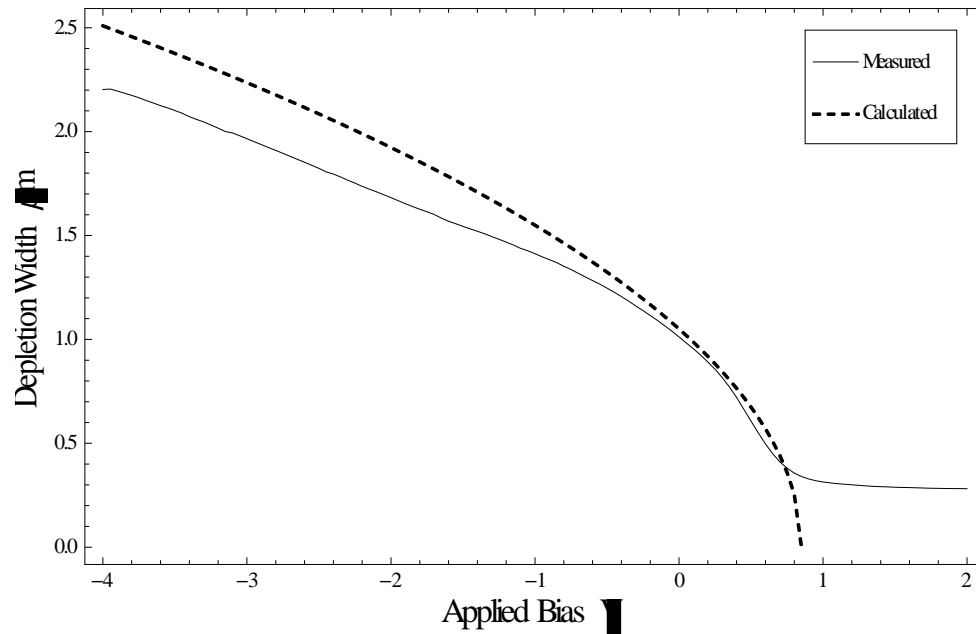
Figure 27. Depletion width of Sample Y3. The depletion width extracted from the C-V data is plotted with the theoretical curve calculated from (13). While the curves do not match exactly, the shape is a good approximation at low reverse biases.

3.4 Experimental Procedure

The experimental procedure consisted of exposing reverse-biased Gd_2O_3 on Si/SiC diodes to a thermal neutron flux in an effort to record neutron interaction induced voltage pulses. The reverse-biased diodes were irradiated in the test fixture with the bare Lexan package and with a layer of Cadmium (Cd) shielding. The Cd shield was employed to absorb a significant amount of the thermal neutrons in an effort to discriminate the neutron induced signal from gamma ray or background induced events.

Initial attempts in the summer of 2010 to replicate results from previous research efforts illuminated several requirements for future experimentation. The wiring of the diodes appeared fragile and great care was required to ensure any BNC connections remain intact when placing the diodes in the pile drawers. This proved quite difficult to accomplish due to the dimensions of the stringers forming the drawers. Figure 28 details a mock stringer, or sled, designed to alleviate any stress on device connections during insertion and removal. This sled allows for accurate replication of placement within the neutron environment. Additionally, a small well in the device area of the sled allows for a liquid nitrogen bath to cool the sample for low temperature in-situ experimentation.

Figure 28. The graphite and Lexan versions of the mock stringer or "sled" created for use in this experiment are shown above as well as the design submitted to the AFIT model and fabrication shop. The dimensions of the sleds are slightly smaller than the standard graphite stringers used to construct the AFIT graphite pile, as well as the OSURR thermal column and sub-critical reactor. These dimensions allow for modularity of experimental set-up and ease of insertion of the detector into the neutron environment.

Fabrication of the sled was delayed, so in the interim, a Lexan version of the sled was fabricated. The remaining Lexan from the sled material was used to create diode packages shown in Figure 29. The Lexan diode packages were originally wired with thin single element wires from the conducting posts to the BNC connector. This wiring configuration was suspected as a source of system noise and the wires were subsequently replaced with short lengths of RG-174 coaxial cable.
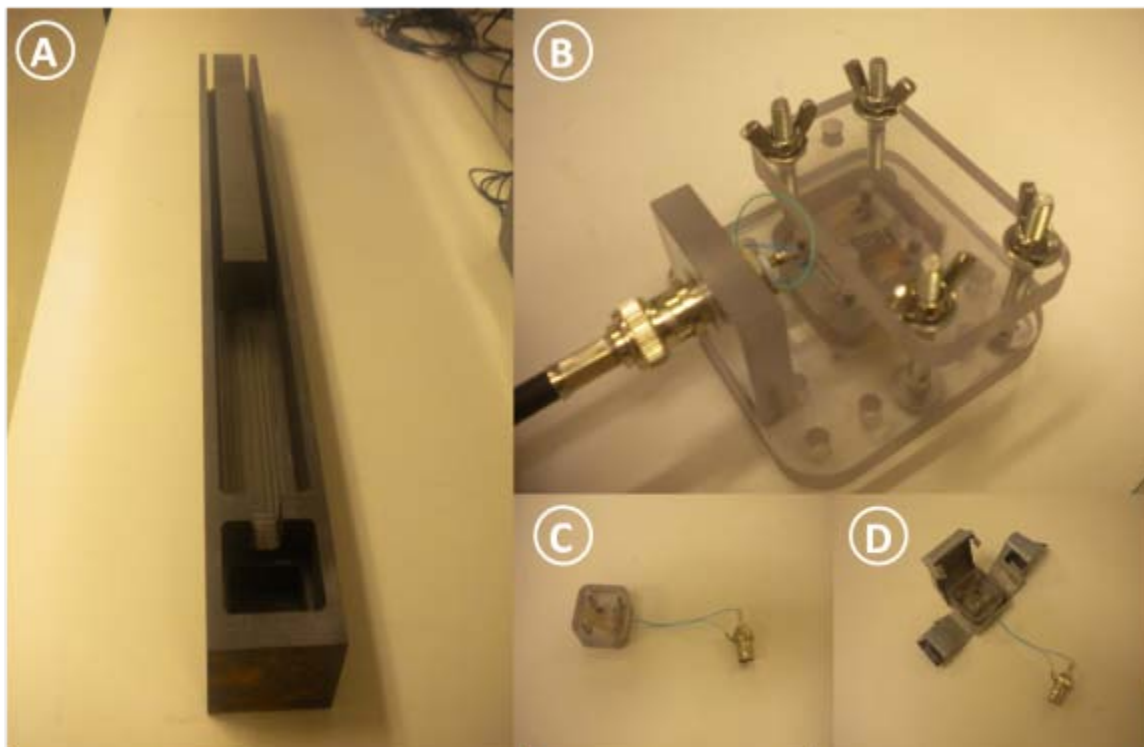
Figure 29. The lower portion of (A) shows the well where the diodes are placed during the experiment. The diodes are packaged in Lexan boxes (C) and then fastened inside a Lexan mount (B) designed to fit in the well shown in (A). (D) shows the diode package in the Cadmium shield. Originally constructed with single wires leading from the conducting posts in the Lexan packages as shown in (B) and (C), the wiring was later changed to RG-174 coaxial cable to eliminate noise induced in the system.

Upon completion of the diode manufacture and characterization, the electronic component apparatus was assembled and tested. The initial configuration consisted of two branches, each with pulse-height discrimination and counting systems routed to a multi-channel analyzer. Two different pre-amplifier models, one in each branch, were employed in this configuration in an effort to determine which provided the optimal characteristics for this experiment. Significant system noise was encountered in the early attempts of the experiment, and various modifications were explored as possible solutions. Most often, the silver paint bond from the device contact broke and created an open circuit.

Small aluminum boxes were fabricated to serve as Faraday cages to help eliminate noise. The boxes proved problematic and were eventually abandoned in favor of aluminum foil. The discrimination and counting system was also abandoned as no data was collected at voltages above that of the system noise. If a neutron signal from the diodes did exist, it was buried in the noise. The final configuration is illustrated in Figure 30.
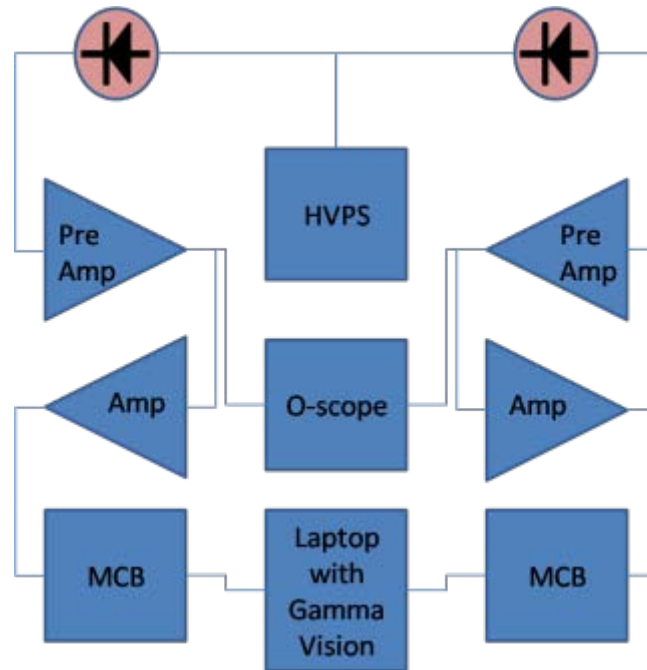
Figure 30. Depiction of the electronics configuration for signal collection from the Gd_2O_3 on Si/SiC diodes. The power from the high voltage power supply is split, allowing for concurrent experimentation of two diodes.

Constructed in 1962, The AFIT Standard Graphite Pile consists of 18 layers of alternating 4" x 4" x 50" reactor grade graphite (AGOT) stringers supported internally by an aluminum frame resting on an aluminum base plate. Standing at just over six feet tall and four feet wide, the stringer lattice and aluminum frame assembly is incased in a wooden housing lined with cadmium to prevent thermal neutron escape and limit neutron

intrusion [26]. The neutron source for the AFIT Pile is a five Curie plutonium-beryllium source with roughly an 8×10^{6} n/ s source strength. The AGOT stringers have a moderating ratio of about 170, moderating the emitted neutrons to a thermal neutron flux on the order 10^{4} n/cm^{2} s in drawer 3 of the pile. Doors are located at various positions around the AFIT Pile housing to allow removal of the stringers for source or experimental apparatus insertion. The construction and drawer location are depicted in Figure 31.
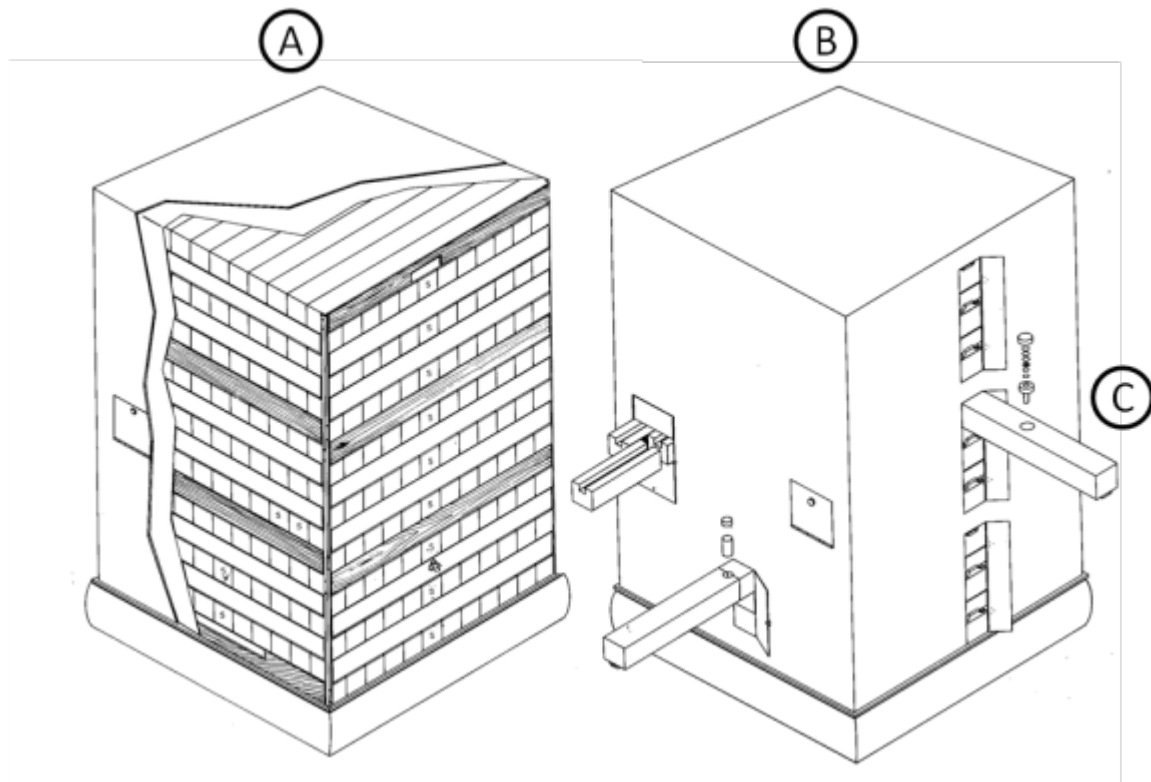
Figure 31. The AFIT Standard Graphite Pile. The AFIT Pile consists of stacked graphite stringers encased in a wooden frame lined with Cadmium (A). As shown in (B), several access panels allow for removal of stringers in insertion of neutron sources such as the AFIT controlled PuBe source. (C) shows a stringer partially removed from drawer 6 [26].

The AFIT Standard Graphite Pile thermal neutron flux was measured via foil activation analysis by AFIT personnel in early 2010. A model of the AFIT Pile using

Geometry and Tracking software (GEANT4) was used to predict the thermal neutron flux

at the various drawer locations. In the interest of efficiency and time, the GEANT4

model was implemented using fewer spontaneous emission events than expected from the

calculated activity of the PuBe source. Despite this scaled down activity, the shape of the

curve generated when plotting the modeled thermal neutron flux versus drawer location

matches the shape of the curve of the measured values as illustrated in Figure 32.
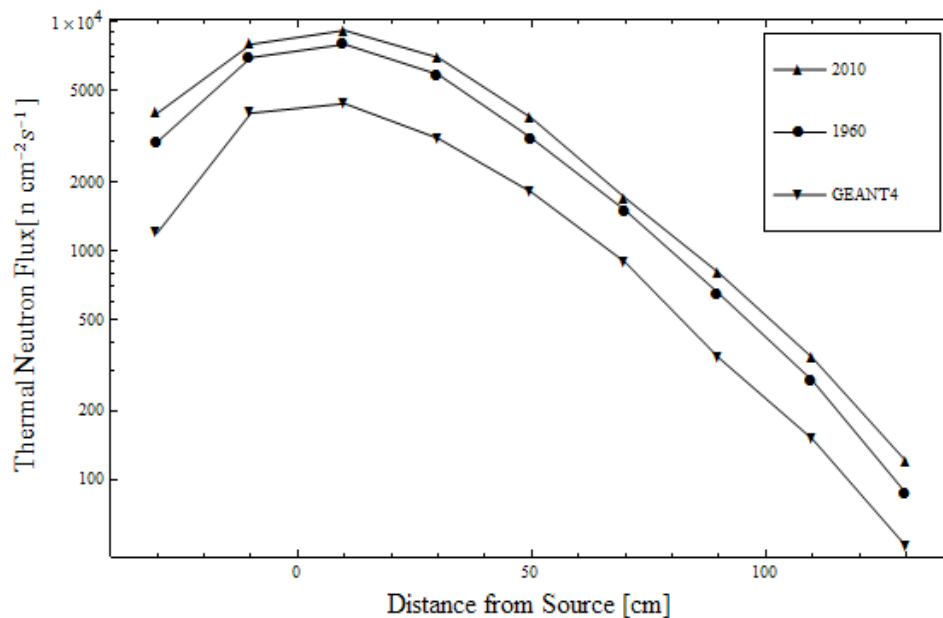
Figure 32. Results of the GEANT4 model of the thermal neutron flux of the AFIT controlled graphite pile compiled by Austin Wallach and James Bevins. The number of events used in the simulation was scaled down from the actual PuBe source activity, however, the shape of the curve matches very well with the flux values measured in 1960 and 2010.

Drawer 6 was determined to be the optimal position for thermal neutron

interaction due to the relatively high flux of thermal neutrons and low gamma incidence

as illustrated in Figure 33. Assuming the diameter of the contacts to be roughly 0.8mm, a

diode placed in drawer 6 could have as many as 50 incident thermal neutrons per second.

However, applying the parameters of Table5 to (15), the incident thermal neutron

interaction with the Gd-157 nuclei may produce approximately 27 79 keV IC electrons per hour.
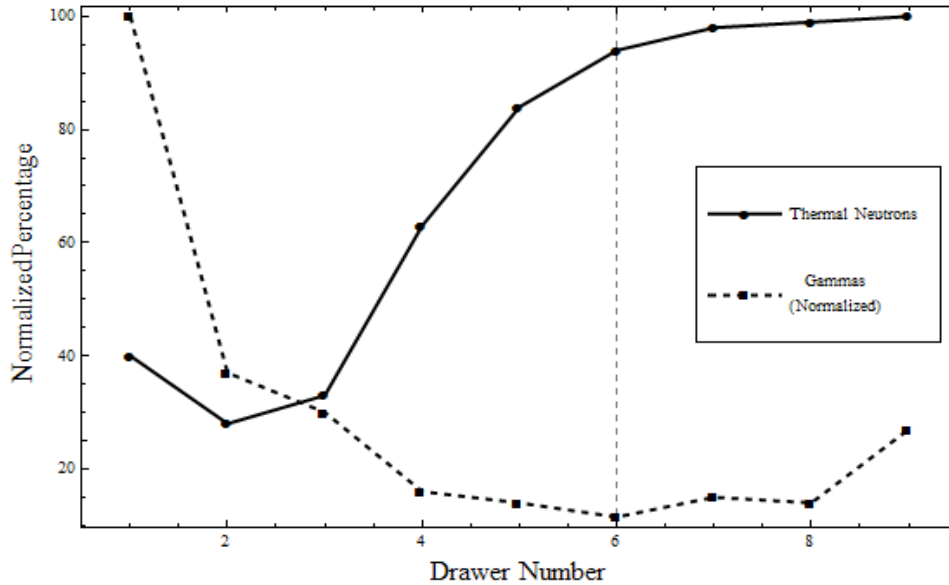
Figure 33. Plot of the GEANT4 results of thermal neutrons and associated gammas by drawer number. Due to the high thermal neutron flux and low percentage of gammas per neutron, drawer 6 was selected as the location for the placement of the experimental diodes.

The Ohio State University Research Reactor (OSURR) is a 500 kW pool-type research reactor utilizing Uranium as the nuclear fuel. Though capable of achieving an output of 500 kW, the power output is limited by regulation to not exceed 450 kW for safety purposes. The core of the reactor resides in a 20 foot deep reactor pool formed from borated concrete. Various access ports allow for experimental apparatus exposure to neutron fluxes as high as 2.3×10^{13} n cm^{-2} s^{-1}. As shown in Figure 34, the thermal column of the OSURR consists of a column of graphite stringers that moderate the fast and epithermal neutrons and create a high thermal neutron flux. With the OSURR operating at the maximum output of 450 kW, the thermal column has a calibrated thermal

neutron flux of approximately 10^{13} n cm^{-2} s^{-1} at positions adjacent to the reactor core and 10^{11} n cm^{-2} s^{-1} near the outside surface.
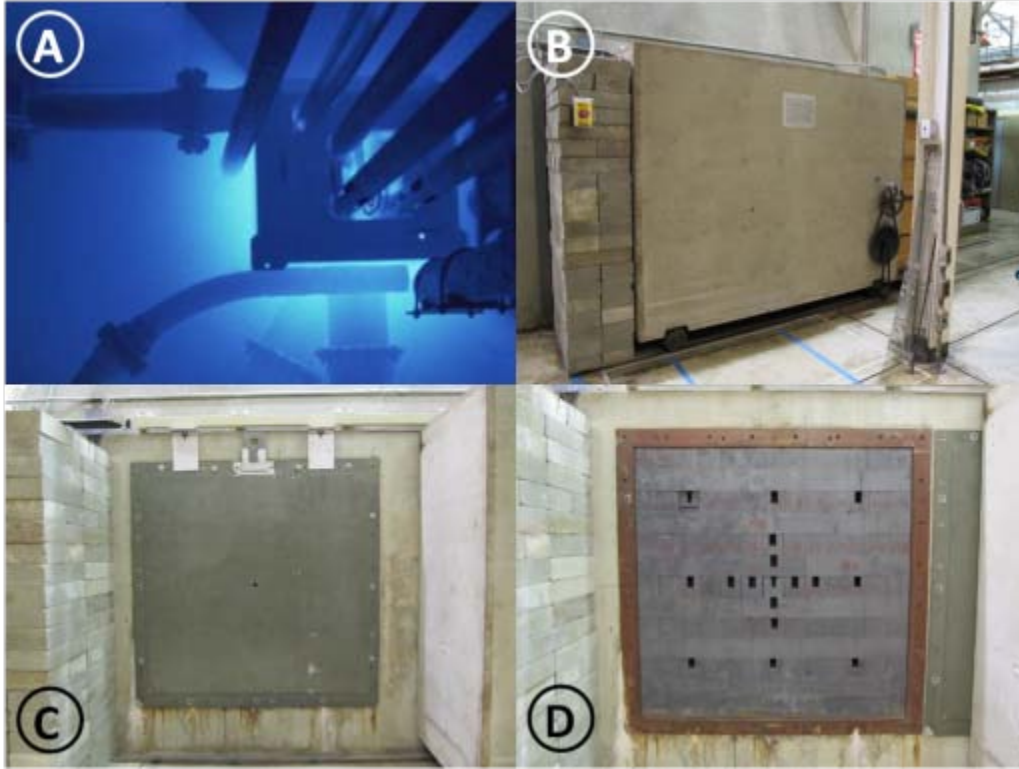
Figure 34. The Ohio State University Research Reactor (OSURR) is a 500 kW pool reactor. (A) shows the reactor vessel as viewed from above and the various experiment ports. The thermal column is adjacent to the wall depicted to the right of the core in (A). The thermal column consists of a graphite stringers (D) shielded by a sliding Boron lined plate (C). The access to the thermal column is further shielded by a borated concrete door that is winched along steel rails (B).

IV. RESULTS AND FINDINGS

4.1 Introduction

Two thermal neutron sources were available for use in this experiment: the AFIT Standard Graphite Pile and the thermal column of the OSURR. The original intention for using two sources was to corroborate any findings from the low flux in the AFIT Pile with the high flux environment of the OSURR. No results requiring corroboration were obtained from the AFIT Pile experiments. Oscilloscope traces and pulse height spectra collected from the OSURR experiment, however, did reveal some interesting features.

4.2 AFIT Standard Graphite Pile

The Si and SiC based diodes were characterized in the AFIT standard graphite pile over the course of several weeks of experiments. Each diode was biased to three different reverse biases with the sled both inside of the drawers and outside of the pile. Spectra were recorded using GammaVision software installed on a laptop computer connected via USB cable to an Ortec 926 MCB. The spectra obtained from 600 second collection runs with sample Y3 are shown below in Figure 35.
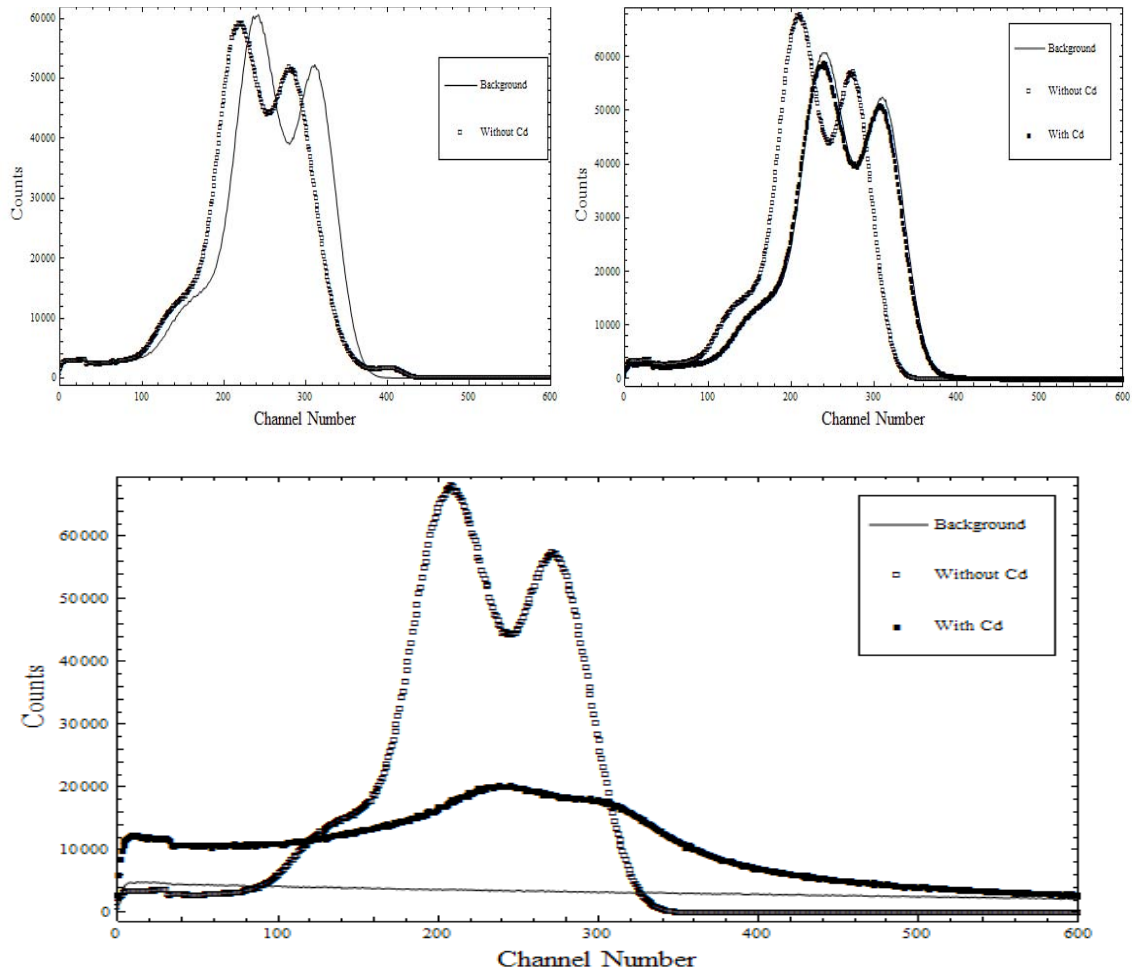
Figure 35. Sample Y3 reverse-biased to 0.5 V (top left), 1.5 V (top right), and 5 V (bottom) with a total collection time of 600 seconds. With the MCB set for 8192 channels, the left peak corresponds to approximately 250 mV while the peak to the right corresponds to approximately 350 mV.

The double peak feature of the spectra collected from sample Y3 appeared to be the most interesting result of the irradiation experiments in the AFIT Pile. No settings on any of the signal collection equipment components were changed for the different collection runs. The disparity in counts in the 5 V reverse bias runs appeared to give promising results. The ratio of counts between background and exposed might suggest some radiation sensitivity, while the ratio of Cd shielded and exposed to unshielded and exposed would suggest neutron interaction in the diode. It is these results that led to the

decision to bring sample Y3 to the OSURR thermal column and expose it to a higher neutron flux.

The same process was repeated with sample T5, a SiC based sample. The results of the 600 seconds pulse height spectrum collection runs are presented below in Figure 36. While no double peak feature was observed with this sample, a reduction in counts occurred in both cases where Cd shielding was applied to the diode. Of particular interest, however, is the disappearance of the peak in both the 1.5 V and 5 V reverse bias irradiations when the Cd shielding was placed on the diode. Again, initial excitement over possible thermal neutron absorption by the Cd shield gave way to skepticism due to the disappearance of the peak. It is possible that the peak observed is due to system generated noise. The Cd shield, then, could serve as a Faraday cage, removing that noise and deleting the feature seen on the spectrum. Regardless of their source, these curious features are the reason samples Y3 and T5 were selected for further exploration in the thermal column of the OSURR.

The peak of the spectrum shown in the lower portion of Figure 36 occurs at approximately channel 1200. Considering the settings of the equipment listed in Appendix B – Equipment and Settings and the measured gain of 3000 for the Ortec 142IH Pre Amplifier, this peak corresponds to 75 nV. With a measured system capacitance of 0.968 pF, the charge deposited in the detector is approximately 7.27×10^{-8} pC.
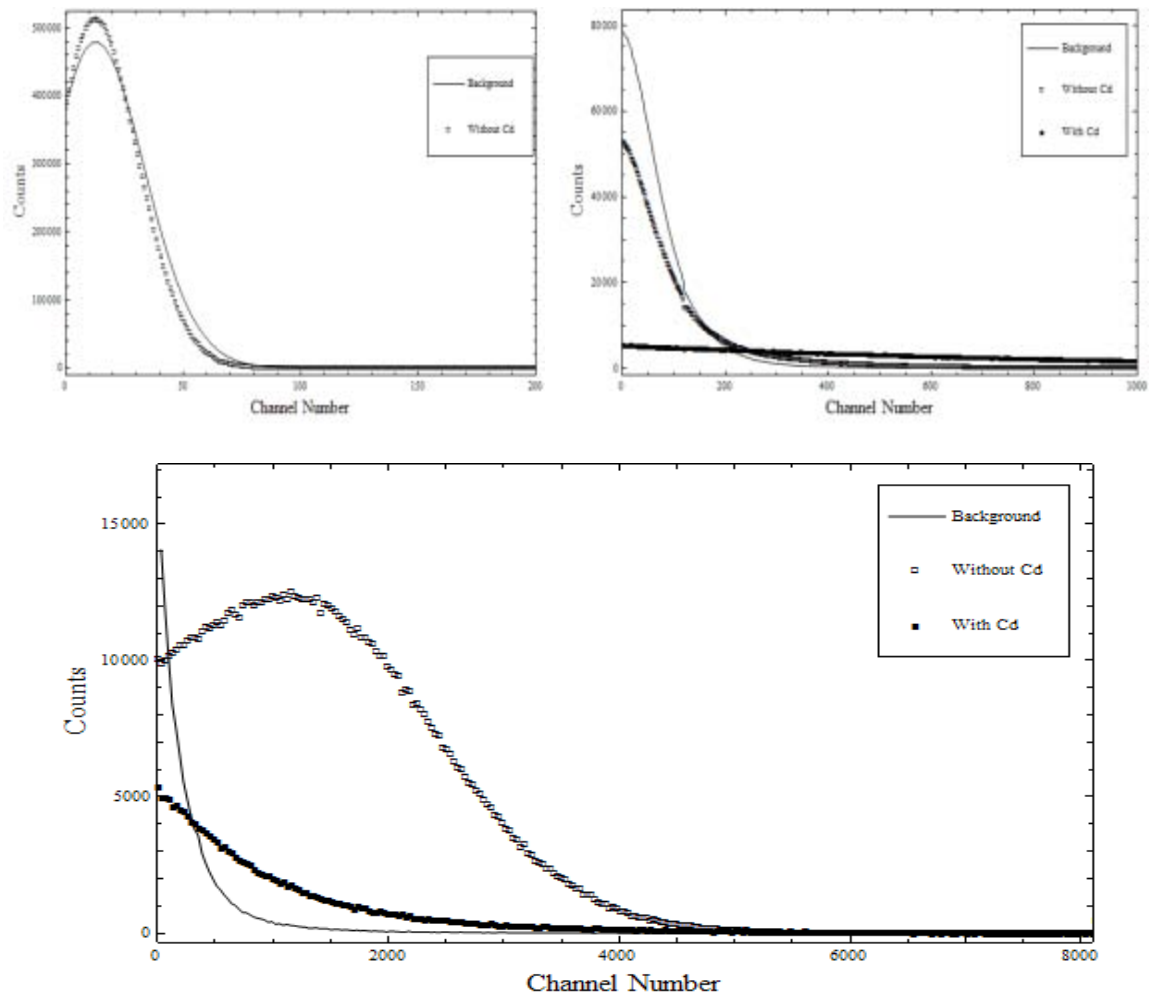
Figure 36. **Sample T5 in the AFIT Standard Subcritical Graphite Pile. The diode was reverse-biased to 5V. The spectrum was collected over 600 seconds.**

4.3 OSURR Thermal Column

The samples were characterized in the thermal column prior to reactor start-up.

Sample T5 was placed in the Lexan sled in position G6 as shown in Figure 37, and

sample Y3 was placed in the graphite sled in position G8. After completing the

background spectrum collection, the reactor was brought to initial power level of 1 kW.

Spectra were collected for 150 seconds at the same reverse-bias voltages used in the

AFIT Pile irradiations. The reactor power was then increased to 10 kW and a spectrum

was collected from the diode reverse-biased to 5 V. The power was then brought down

to a level allowing access to the thermal column, and Cd shields were placed on the

diodes. The thermal column access was once again sealed and the measurement process

repeated.
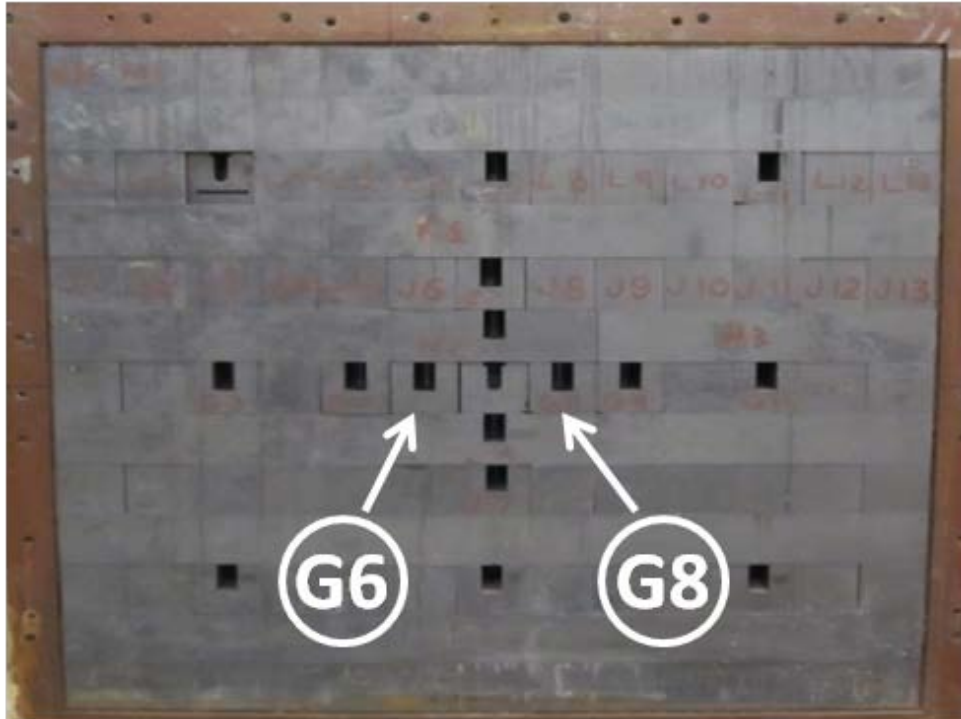
Figure 37. The various stringers of the thermal column. The Lexan sled with sample T5 was placed in the G6 position, while the graphite sled was inserted into G8. The cabling was routed out of the sleds and taped to the ends of the stringers to allow the access plate and concrete door to seal the thermal column during operation.

Figure 37 shows the spectra obtained in 150 second collections with sample Y3 at

different reverse-biases. There appears to be little relative change in the spectra between

the different bias irradiations and reactor power output levels.
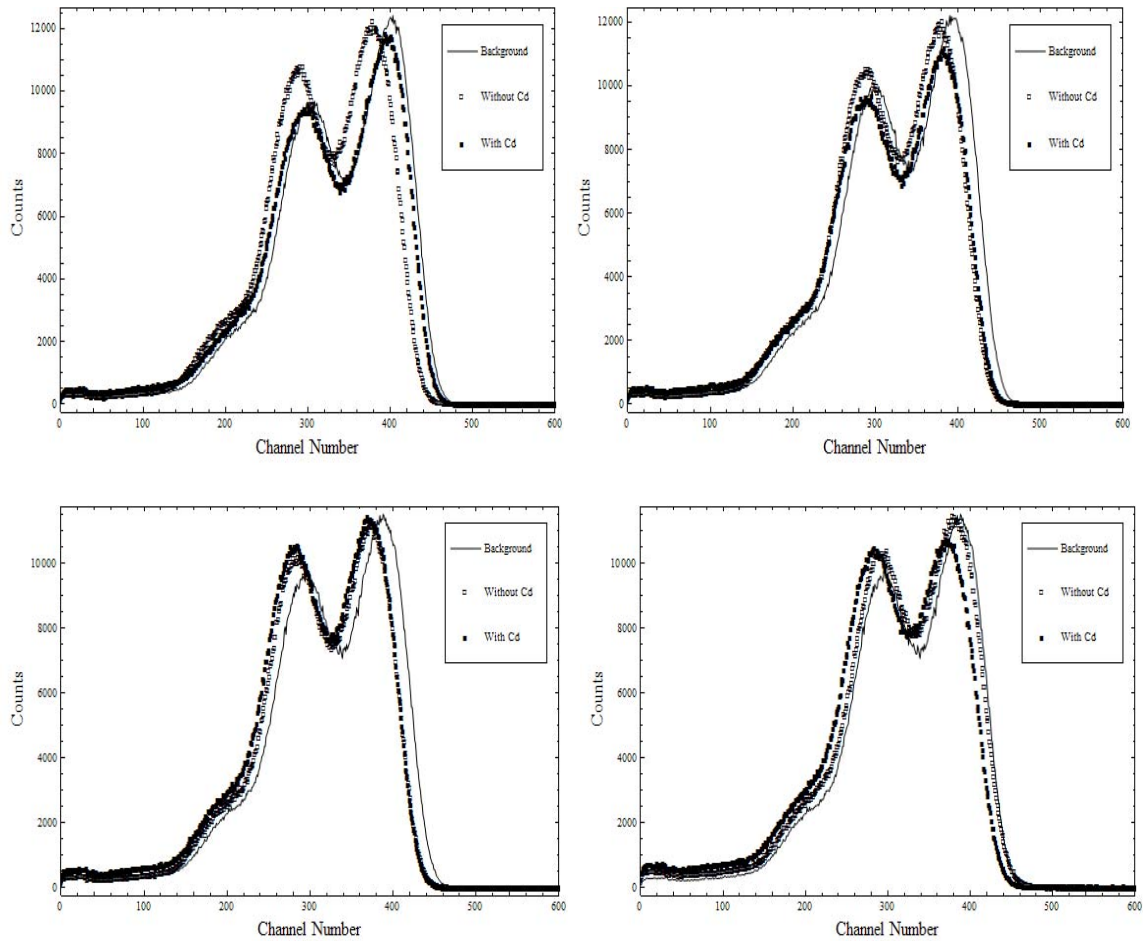
Figure 38. Sample Y3 reverse-biased to 0.5 V (top left), 1.5 V (top right), and 5 V (bottom left) with the reactor running at 1 kW. Sample Y3 reverse-biased to 5 V and the reactor running at 10 kW of output power is shown (bottom right).

It was later discovered through I-V characterization that the wire bond on the contact of sample Y3 had broken during the irradiation. The open circuit noise is thought to have created the double peak feature evident in the OSURR spectra, as well as the AFIT Pile spectra. The post-AFIT Pile irradiation I-V traces are shown in Figure 39.
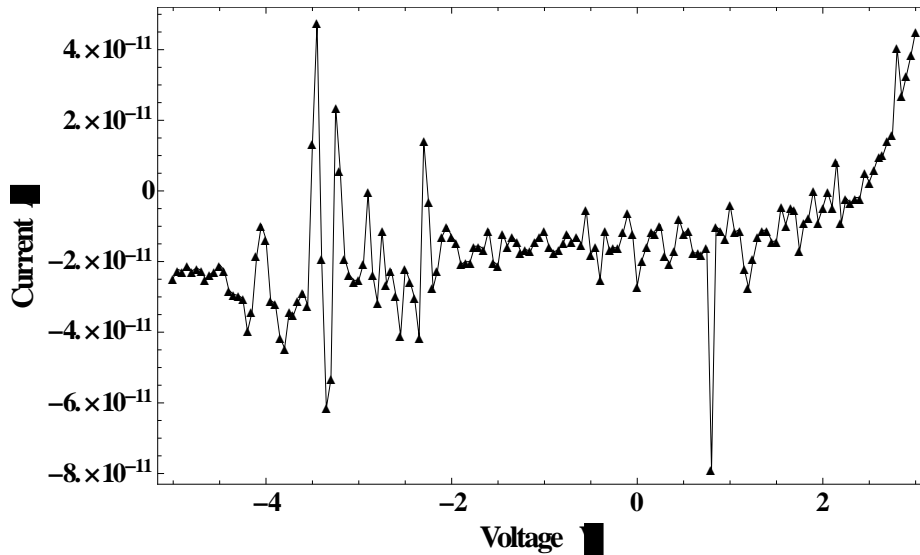
Figure 39. I-V measurements of sample Y3 taken after the AFIT Pile irradiation but prior to the OSURR thermal column irradiation. The data was taken but not analyzed until after the OSURR irradiation. Analysis of the spectra collected suggests that the gold wire broke loose from the silver painted bond to the contact during the 5 V reverse bias run of the AFIT Pile irradiation.

Spectra collected from sample T5 show the same decrease in counts between shielded and bare irradiations; however, the peak remains present in the shielded runs at the lower reverse bias voltages as plotted in Figure 40. The background signal also displays this peak, suggesting the peak is a result of system noise. The peaks appear to shift to lower channels with increased reverse-bias. At 5 V reverse-bias the Cd shielded peak disappears and re-appears when the reactor power level is increased to 10 kW. This shifting of the features with the changes in parameters once again suggests that the peaks in the pulse height spectra are a result of the system generated or system amplified noise.
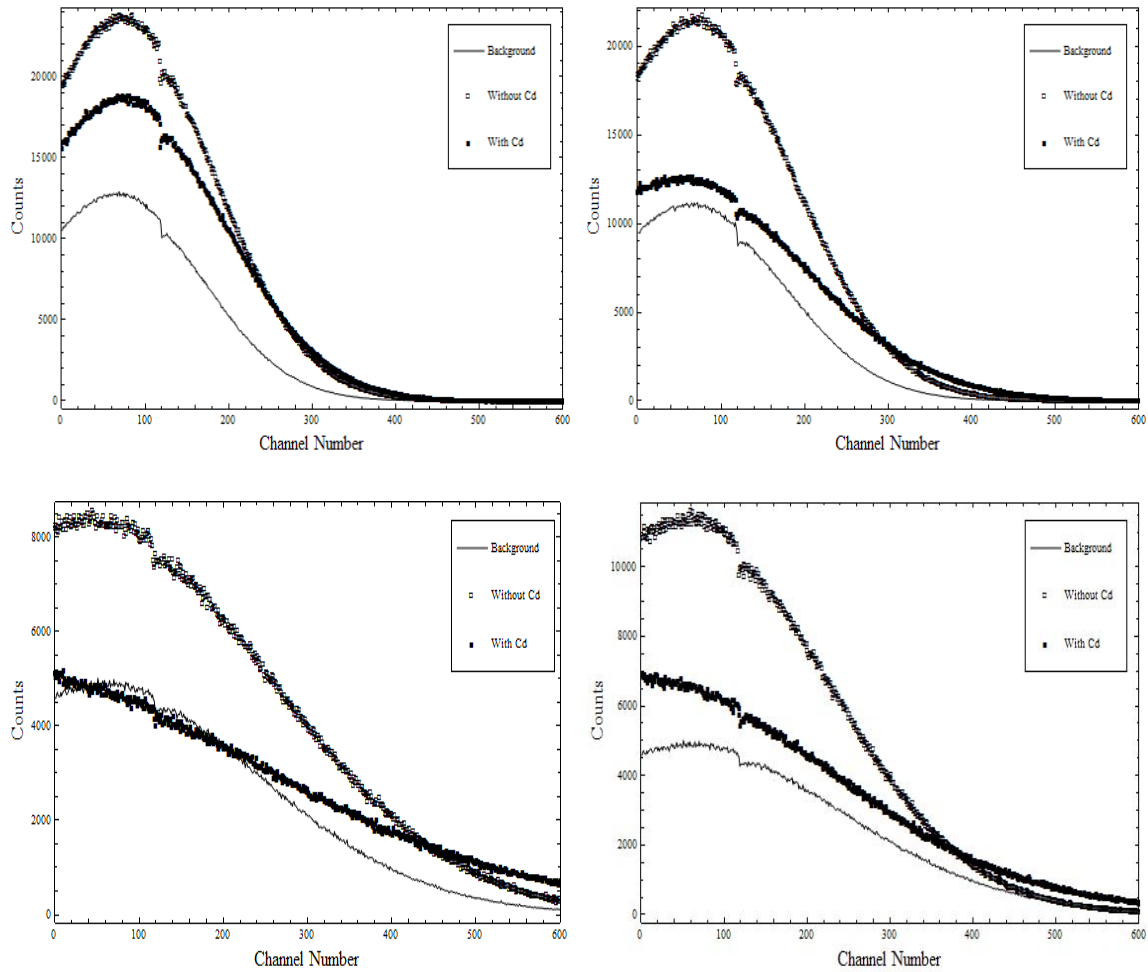
Figure 40. Sample T5 reverse-biased to 0.5 V (top left), 1.5 V (top right), and 5 V (bottom left) with the reactor running at 1 kW. Sample T5 reverse-biased to 5 V and the reactor running at 10 kW of output power is shown (bottom right).

During the course of spectra collection, the pre-amp output was displayed on the oscilloscope. During the 5 V reverse-bias irradiation at a reactor output power of 1 kW, an intermittent pulse was detected on the oscilloscope trace for sample T5. A screen capture of this pulse as well as the output of a pulser signal from the pre-amp is shown in Figure 41.
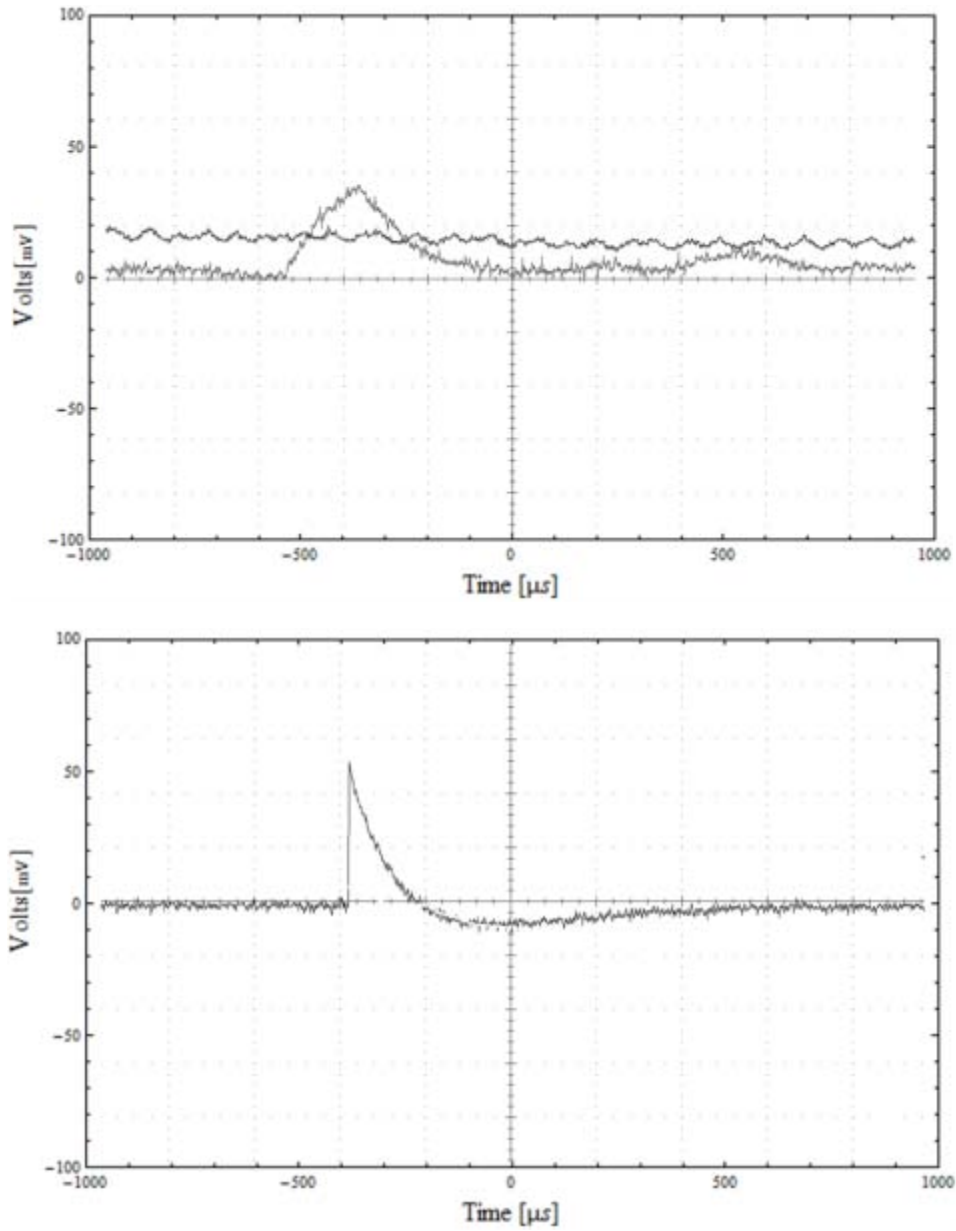
Figure 41. Oscilloscope Traces during the neutron irradiation with the reactor at 10 kW output power. (Top) Both sample Y3 and T5 are displayed. The diodes were reverse-biased to 5 V. The noise creating the characteristic double peak in the Y3 pulse height spectrum is seen overlaid on a possible radiation induced pulse in sample T5. (Bottom) Oscilloscope trace of a pulser output from the Ortec 142IH Preamp.

The pulse decays over the same period as the tail of the pulser signal. While the

pulses appeared to have a completely random frequency, the shape of the pulse varied

from a sharp pulse to piled pulses. As the charge created by the collection of one pulse

63

decayed from the pre-amp, another pulse was collected and the charge was summed with the remaining charge from the previous pulse. An example of the observed pile-up pulses is shown in Figure 42.
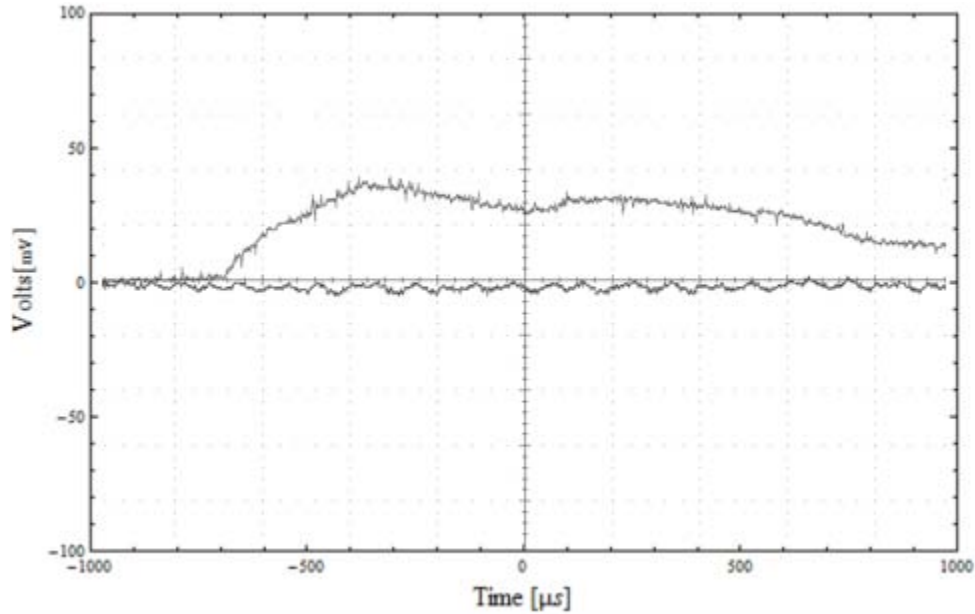
Figure 42. Possible pulse pile-up during the 10 kW output irradiation with the diodes reverse-biased to 5 V.

The pulses observed, and shown in Figure 41 and Figure 42, do not contribute to any discernable peak in the collected pulse height spectra. The pulses were observed at a rate of approximately 1 pulse every 4 to 5 s. Over the course of a 150 s spectrum collection, these pulses would contribute roughly 35 counts to their respective voltage bins. It was assumed that high counts at the low end of the spectrum are the result of the system generated noise. These high numbers of noise counts masked any features in the spectra attributable to the observed pulses.

The equipment inserted into the thermal column during the first iteration of the experiment experienced significant activation due to trace amounts of copper, as well as

gold and the other materials of the samples and equipment. These pieces of equipment were left in a lead vault on the OSURR grounds for approximately one month to decay. The experiment was then repeated to determine the effect of the thermal neutron flux on the rate of observed pulses. The noise at the low end of the spectrum was discriminated out using the lower level discriminator on the MCB. Figure 43 shows the pulse height spectra collected from sample Y11 over the course of 300 s collection runs with the reactor running at output power levels of 1 kW, 10 kW, and 100 kW.
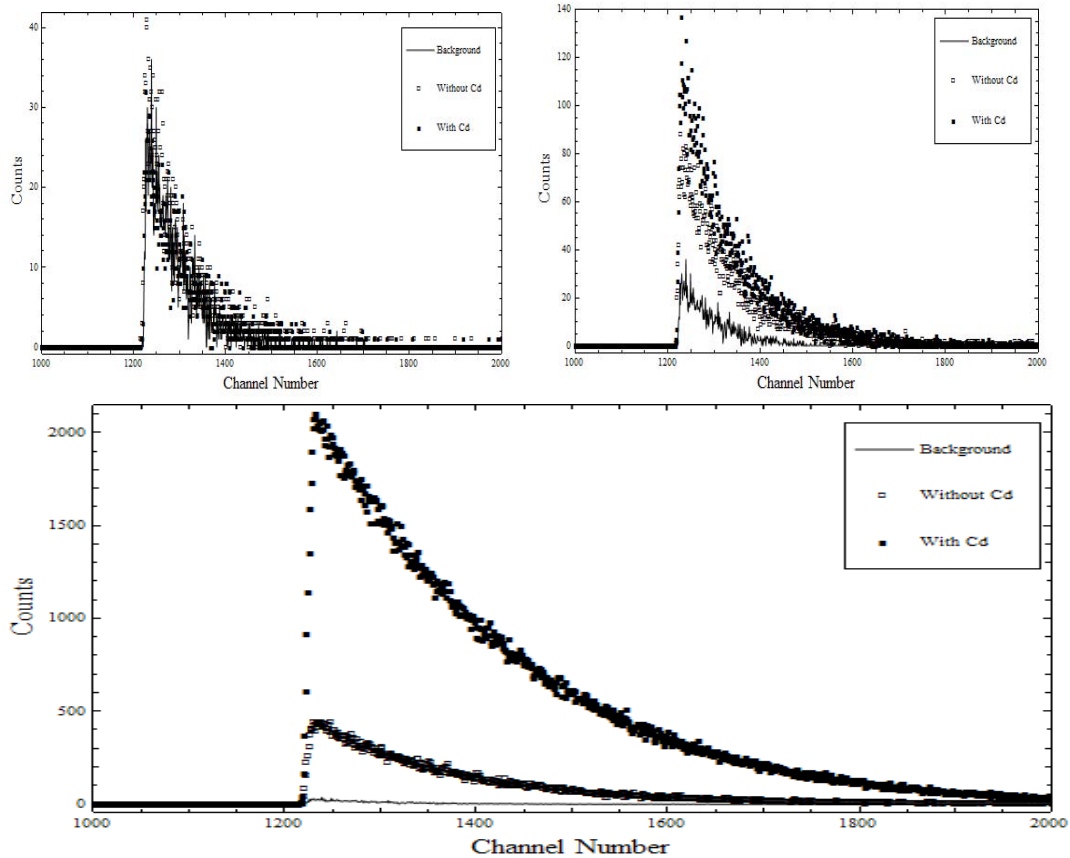
Figure 43. Pulse height spectra from sample Y11 collected over 300 s. The spectra were collected with the OSURR running at a power output of 1 kW (top left), 10 kW (top right) and 100 kW (bottom). The Cd shielding generally increased the count rate at power levels of 10 kW and 100 kW.

The number of counts appears to increase with the addition of the Cd shielding. This is consistent with the results obtained from the irradiation of sample T5, though not immediately obvious. Figure 44 shows the spectrum collected from sample T5 reverse-biased to 5 V with the reactor running at 10 kW of output power. While the peak of the distribution is much higher for the bare diode, closer inspection of the tail of the distribution reveals the same higher count rate for the Cd shielded diode versus the bare diode. Therefore, had the lower end of the spectrum not been removed by discrimination via the MCB, one would observe a higher aggregate number of counts from the bare diode relative to the Cd shielded diode.
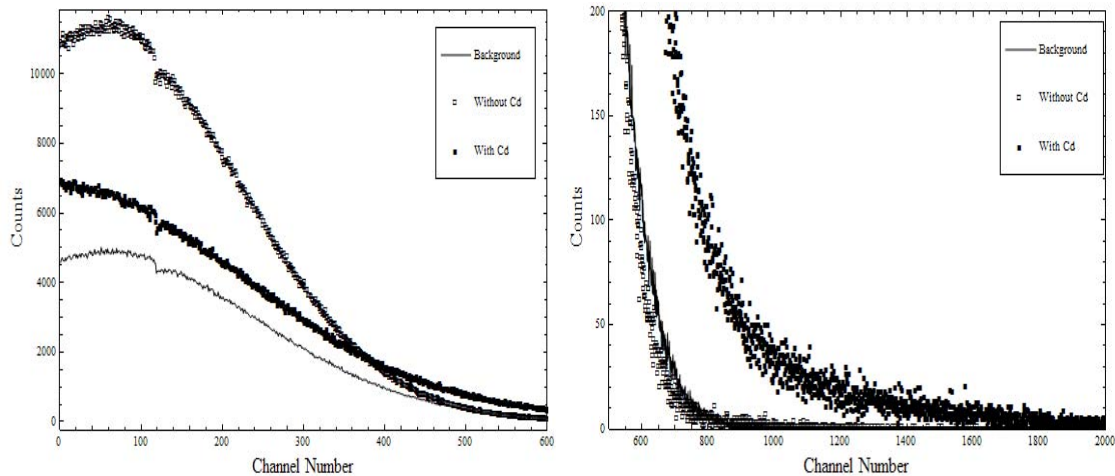
Figure 44. The tail of the peak of the pulse height spectrum collected from sample T5. The detector was reverse-biased to 5 V and the reactor was running at an output power of 10 kW. As shown to the left, the aggregate number of counts collected from the Cd shielded diode is much less than that collected from the unshielded diode. At the tail of the distribution, however, the number of counts per channel from the Cd shielded diode exceeds that of the unshielded.

Pulses similar to those observed with sample T5 were once again observed from sample Y11. The pulses appeared at roughly one pulse every 4 to 5 s, independent of reactor power output and, consequently, thermal neutron flux. Samples of the pulses

observed are shown below in Figure 45. The observed pulses have a much faster rise time than those collected in the first iteration of the experiment. The pulses were observed in both the bare exposure in the thermal column and the Cd shielded exposure, indicating that pulse is most probably not due to thermal neutron interaction with a Gd-157 nucleus.
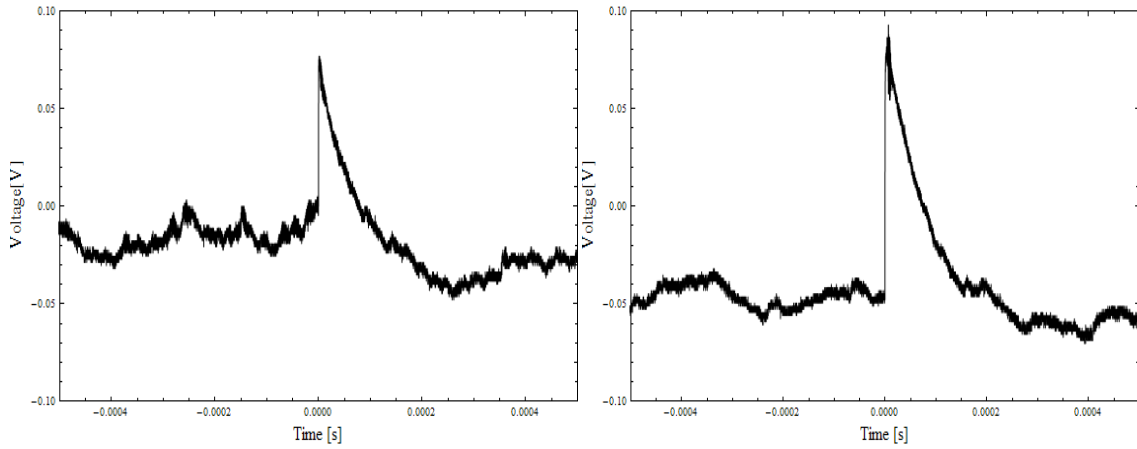
Figure 45. Pulses collected from sample Y11 with the reactor running at an output power level of 100 kW. The pulse on the left was collected from the unshielded diode, while the pulse on the right was collected from the Cd shielded diode.

V. CONCLUSIONS AND RECOMMENDATIONS

Neutron detection utilizing Gd_2O_3 on Si or Gd_2O_3 on SiC diodes was not accomplished during this research effort. The pulses captured on the oscilloscope are the result of ionization in the depletion width of the reverse-biased diode, there is no evidence to support a claim that these signals were created as a result of neutron interaction with the Gd_2O_3 conversion layer. While theory supports the feasibility of neutron detection with these diodes, device fabrication constraints have so far limited their realization as detectors.

A disproportionate amount of effort and attention was devoted to device fabrication. The need for new methods to overcome the familiar obstacles of wire bonding and sample packaging was recognized early in the course of the research. While multiple packages and bonding techniques were attempted, no satisfactorily complete solution was ever achieved. Optimal diode characteristics could be achievable through isolation of the contacts with a silicon dioxide (SiO_2) insulation layer. Additionally, ultrasonic wire-bonding to contacts of thickness sufficient to promote bonding while preventing the needle from punching through will provide a connection with minimal noise.

The initial high number of counts at the low end of the pulse-height spectra collected during the experimentation portion of this research masked any detection signal that may have been present. Subsequent attempts at noise discrimination by the electronic signal collection configuration failed to reveal any discernable features in the collected

68

spectra. Changes in the count collection rate with the various reactor power settings suggest that the diode displays radiation sensitivity. This sensitivity could be tested with a series of experiments employing mono-energetic radiation sources such as strontium-90 or cobalt-57 [3].

The results from the CASINO modeling effort indicate that a very small percentage of the IC electrons would fully deposit their energy within the achievable active detector volume. Meanwhile, all of the IC electrons, as well as all of the associated gamma rays and any background radiation, deposit some fraction of their energy in the active volume as they transit through the detector. This distribution of energy deposited in the detector effectively drowns out any spectral peak created by the relatively miniscule number of full deposition events. Better device construction will allow for lower leakage current at greater reverse bias voltages. If the diode could be depleted such that nearly all of the IC electrons would fully deposit their energy within the depletion region, a discernable peak could possibly be observed in the pulse height spectrum. The question remains whether the diode can be biased to full depletion without experiencing breakdown. The Davinci simulation did not predict breakdown at reverse-bias voltages of 30 V, however, greater voltages were not explored due to the measured leakage currents from the actual diodes.

The Davinci code created during this research proved insufficient at modeling the response of the diodes to charge carrier deposition. This failure is based on the limitation of 30,000 nodes. A 2D Davinci simulation would allow for modeling a much larger cross-section of the diode, and, therefore, a much greater transfer of energy from the

69

incident IC electron. Other available software, particularly GEANT4, allows for simulation of the neutron interaction and subsequent IC electron emission as well as full scale modeling of the device and charge carrier deposition.

Finally, low temperature characterization of one of these samples shows that at a temperature of 80 K and an applied reverse bias of 2 V, the leakage current was reduced by approximately three orders of magnitude. While the mobility of the charge carriers is greatly increased at these low temperatures, the defect energy levels that serve as tunneling sites at room temperature no longer have enough thermal energy to accept these electrons. Thus the decreased tunneling probability results in significantly lower leakage current at low temperature. The reduced leakage current should allow for a greater applied reverse bias, and therefore a larger depletion region in which to collect charge. The graphite sled created for this research allows for a liquid nitrogen bath. Low temperature measurement collection should be explored as a means to improve diode characteristics.

VI. APPENDICES

Appendix A – Sample Index

The samples used in this experiment were tracked using the following table:

Sample	# Contacts	Packaged?	By Who	Recipe	Deposited By
Y11	4	N		4	AFRL
Y12	4	N		4	AFRL
Y13	4	N		4	AFRL
Y14	6	Y	AFRL	1	UNL
Y15	6	Y	AFRL	1	UNL
Y16	5	Y	AFRL	1	UNL
Y21	6	Y	AFRL	1	UNL
Y22	2	Y	AFRL	1	UNL
Y23	4	N		1	UNL
Y24	4	Y	ME	1	UNL
Y25	6	Y	AFRL	1	UNL
Y26	2	Y	AFRL	1	UNL
Y3	A-5	N		1	UNL
	B-5			1	UNL
	C-5			1	UNL
Y4	10	N		1	UNL
YX1	2	N		3	AFRL
YX2	4	N		4	AFRL

YX3	3	Y	AFRL	3	AFRL
YX4	3	N		4	AFRL
YX5	4	N		4	AFRL
YX6	4	N		4	AFRL
T1	2	N		3	AFRL
T2	4	Y	AFRL	3	AFRL
T3	2	Y	AFRL	3	AFRL
T4	4	Y	AFRL	2	AFIT
T5	4	N		2	AFIT

Appendix B – Equipment and Settings

Equipment List

Component	Model	Serial # Graphite Sled	Serial # Lexan Sled
Oscilloscope	Tektronix DPO7104	B022189	
Laptop	Gateway w/ GammaVision	40350828	
HVPS	MASTECH HY3006D	237706	
Linear Amplifier	Ortec 572A	536	3645
MCB	Ortec 926	339	6165198
PreAmp	Ortec 142IH	2034	
	Ortec 142PC	1686	
	Amptek A250CF		1537
	Amptek A250CF		1521
Voltage Regulator	Tripp-Lite LCR-2400	9616AYOLC615000208	
Pulser	Ortec 480	2392	

Settings

Graphite Sled

MCB	8192 channels	
Pre-Amp	AmpTek CoolFET	1537
Linear Amp	FG	6.5
	CG	200
	Shaping Time	3 µs

Lexan Sled

MCB	8192 channels	
Pre-Amp	AmpTek CoolFET	1537
Linear Amp	FG	6.5
	CG	1000
	Shaping Time	3 µs

Appendix C – Davinci Codes and Plots

The Gd_2O_3 on Si model input code is shown below.

TITLE   Gd2O3 on Si Final Version

$Defining the Mesh

MESH

X.MESH X.MAX=3.0 N.SPACES=10

Y.MESH Y.MIN=0.0 Y.MAX=0.2 N.SPACES=60

Y.MESH Y.MIN=0.2 Y.MAX=0.5 N.SPACES=60

Y.MESH Y.MIN=0.5 Y.MAX=2.0 N.SPACES=30

Y.MESH Y.MIN=2.0 Y.MAX=3.0 N.SPACES=10

Z.MESH Z.MAX=3.0 N.SPACES=10

$Defining the region materials and electrodes

REGION   NAME=Substrate X.MAX=3 Y.MIN=.1 Y.MAX=3 Z.MAX=3 SILICON

REGION   NAME=Layer X.MAX=3 Y.MAX=.1 Z.MAX=3 SEMICOND

ELECTR   NAME=Anode   TOP

ELECTR   NAME=Cathode BOTTOM

$Setting the doping profiles for the layer and substrate

PROFILE   REGION=Layer N-TYPE   N.PEAK=5.0E19   UNIF

PROFILE   REGION=Substrate P-TYPE   N.PEAK=1.0E15   UNIF

$Defining the Models used in the simulation

MODELS   SRH AUGER FLDMOB BGN CCSMOB IMPACT.I

MATERIAL SILICON TAUN0=1e-6 TAUP0=1e-6

$ + TUNLN=4E-10 TUNLP=4E-10

MOBILITY SILICON MUN0=1450   MUP0=505

MATERIAL SEMICOND EG.MODEL=3 EG300=3.6 TAUN0=1e-8 TAUP0=1e-8

$ + TUNLN=4E-10 TUNLP=4E-10

MOBILITY SEMICOND MUN0=1400 MUP0=500

$IMPURITY NAME=GB REGION=Substrate

$ + GB=4.0 EB0=0.045 ALPHA=3.037e-8 BETA=200.0 GAMMA=0.950

$ + HDT.MIN=1.0e18 HDT.MAX=1.0e19

$IMPURITY NAME="Ndefects" REGION=Layer

$ + GB=2.0 EB0=0.044 ALPHA=3.100e-8 BETA=200.0 GAMMA=1.000

$ + HDT.MIN=1.0e18 HDT.MAX=1.0e19

$TRAP E1=0.2 TAUN="1E-5" TAUP="1E-6" N.TOT="1e14" COND="@FNENER=1"

$TRAP E2=-0.3 TAUN="3E-5" TAUP="5E-6" N.TOT="-1E13" COND="@FNENER=2" TIMEDEP

$SYMB GUMMEL CARRIERS=0

$METHOD   DAMPED ICCG

$CONTACT   NAME=Cathode RESIST=4.0E3 CAPAC=0.25E-13 PRINT

$LOG   OUT.FILE=DVEX4I

SYMBOL   NEWTON CARRIERS=2

$Creating and Plotting the solutions

PLOT.3D   BOX GRID FILL SCALE CAMERA=(-10,-10,-20)

SOLVE INIT

SOLVE IMPACT.I ELECTRODE=Cathode VSTEP=-.1 NSTEP=10

SOLVE IMPACT.I ELECTRODE=Cathode VSTEP=-.1 NSTEP=40

PLOT.1D POTENTIAL X.START=1.5 X.END=1.5 Y.START=0 Y.END=6 Z.START=1.5 Z.END=1.5

PLOT.1D E.FIELD X.START=1.5 X.END=1.5 Y.START=0 Y.END=6 Z.START=1.5 Z.END=1.5

SOLVE IMPACT.I ELECTRODE=Cathode VSTEP=.1 NSTEP=40

$SOLVE IMPACT.I ELECTRODE=Cathode VSTEP=.05 NSTEP=10

SOLVE IMPACT.I ELECTRODE=Cathode VSTEP=.05 NSTEP=40

$SOLVE IMPACT.I ELECTRODE=Cathode VSTEP=.01 NSTEP=150

SOLVE IMPACT.I ELECTRODE=Cathode VSTEP=.1 NSTEP=20

$SOLVE IMPACT.I ELECTRODE=Cathode VSTEP=.1 NSTEP=20

PLOT.1D Y.LOG X.AXIS=V(Cathode) Y.AXIS=I(Cathode) COLOR=2
     + out.file=FinalJan6.dat

An example of the Photogen code used to inject electron-hole pairs into the simulated diode is given below.

TITLE   THOMAS RESEARCH IONIZATION MODEL

$Defining the Mesh

MESH ^DIAG.FLI

X.MESH X.MAX=3.0 H1=0.20 H2=0.5

Y.MESH Y.MAX=3.0 H1=0.15 H2=0.5

Z.MESH Z.MAX=3.0 H1=0.20 H2=0.5

$Defining the region materials and electrodes

REGION   NAME=Substrate X.MAX=3 Y.MIN=.1 Y.MAX=3 Z.MAX=3 SILICON

REGION   NAME=Layer X.MAX=3 Y.MAX=.1 Z.MAX=3 SEMICOND

ELECTR   NAME=Anode   TOP

ELECTR   NAME=Cathode   BOTTOM

$Setting the doping profiles for the layer and substrate

PROFILE P-TYPE N.PEAK=1.0E15 UNIF   OUT.FILE=DVEX4DS

PROFILE   REGION=Layer N-TYPE   N.PEAK=5.0E19   UNIF

$PROFILE   REGION=Substrate P-TYPE   N.PEAK=1.0E15   UNIF

REGRID DOPING LOG RAT=3 SMOOTH=1 IN.FILE=DVEX4DS

+ OUT.FILE=DVEX4MS

PLOT.3D BOX GRID TITLE="Si Simulation Mesh ReGrid"

+ FILL SCALE CAMERA=(-10,-10,-20)

$Defining the Models used in the simulation

MODELS   SRH AUGER FLDMOB BGN CCSMOB IMPACT.I

MATERIAL SILICON TAUN0=1e-7 TAUP0=1e-7

$ + TUNLN=4E-10 TUNLP=4E-10

MOBILITY SILICON MUN0=1450 MUP0=505

MATERIAL SEMICOND EG.MODEL=3 EG300=3.6 TAUN0=1e-7 TAUP0=1e-7

$ + TUNLN=4E-10 TUNLP=4E-10

MOBILITY SEMICOND MUN0=1400 MUP0=500

SYMB   GUMMEL CARRIERS=0

METHOD   DAMPED ICCG

CONTACT   NAME=Anode RESIST=4.0E3 CAPAC=0.25E-13 PRINT

$LOG   OUT.FILE=DVEX4I

SYMBOL   NEWTON CARRIERS=2

SOLVE

METHOD   ITLIMIT=10

$Creating the solutions

SOLVE V(Cathode)=-5.0

$Injecting the conversion electron to simulate the IC electron

PHOTOGEN   DCHR=0.2 T0=3.0E-12 TC=1.5E-12 LETFILE=dve182let PC.UNITS

SOLVE TSTEP=0.5E-12 TSTOP=1.0E-10

> **+ OUT.FILE=DVE4S01**

$Plotting the results

PLOT.1D   X.AXIS=TIME Y.AXIS=I(Anode) BOTTOM=-2E-3 COLOR=2 TITLE="Current v TIME"

> **+ OUT.FILE=SIion1**

PLOT.1D   X.AXIS=TIME Y.AXIS=V(Anode) COLOR=2 TITLE="Voltage v TIME"

> **+ OUT.FILE=SIion2**

PLOT.1D   X.AXIS=TIME Y.AXIS=I(Anode) INTEG BOTTOM=-4E-14 COLOR=2 TITLE="Collected Charge v TIME"

> **+ OUT.FILE=SIion3**

The internal device characteristics were explored with the following code:

Title   Silicon Model Internal Behavior

$Read in the simulation structure

MESH   IN.FILE=DVEX4MS

LOOP   STEPS=4

ASSIGN NAME=FILE C1=DVE4S02 C2=DVE4S07 C3=DVE4S18 C4=DVE4S28

ASSIGN NAME=TIME C1=1.0 C2=3.4 C3=17 C4=100

$Now Load the Solution File

LOAD IN.FILE=@FILE

$Plot the internal hole and potential distributions

PLOT.3D BOX TITLE="Holes & Potential, "@TIME" psec" SCALE

> **+ CAMERA=(-10,-10,-20)**

CONTOUR HOLE LOG FILL MIN=4.0 DEL=2.0

CONTOUR POTENTIA MIN=-4.0 DEL=0.5 COLOR=1

```
PLOT.3D  BOX  BOUND  SCALE  CAMERA=(-10,-10,-20)

        + ^CLEAR  TITLE=" "

L.END

LOOP    STEPS=4

ASSIGN NAME=FILE  C1=DVE4S02  C2=DVE4S07  C3=DVE4S18  C4=DVE4S28

ASSIGN  NAME=TIME  C1=1.0  C2=3.4  C3=17  C4=100


$Now Load the Solution File

LOAD  IN.FILE=@FILE


$Plot the internal hole and potential distributions

PLOT.3D  BOX  TITLE="Electrons & Potential, "@TIME" psec"  SCALE

        + CAMERA=(-10,-10,-20)

CONTOUR  ELECTRON  LOG FILL  MIN=4.0  DEL=2.0

CONTOUR  POTENTIA  MIN=-4.0  DEL=0.5  COLOR=1

PLOT.3D  BOX  BOUND  SCALE  CAMERA=(-10,-10,-20)

        + ^CLEAR  TITLE=" "

L.END
```
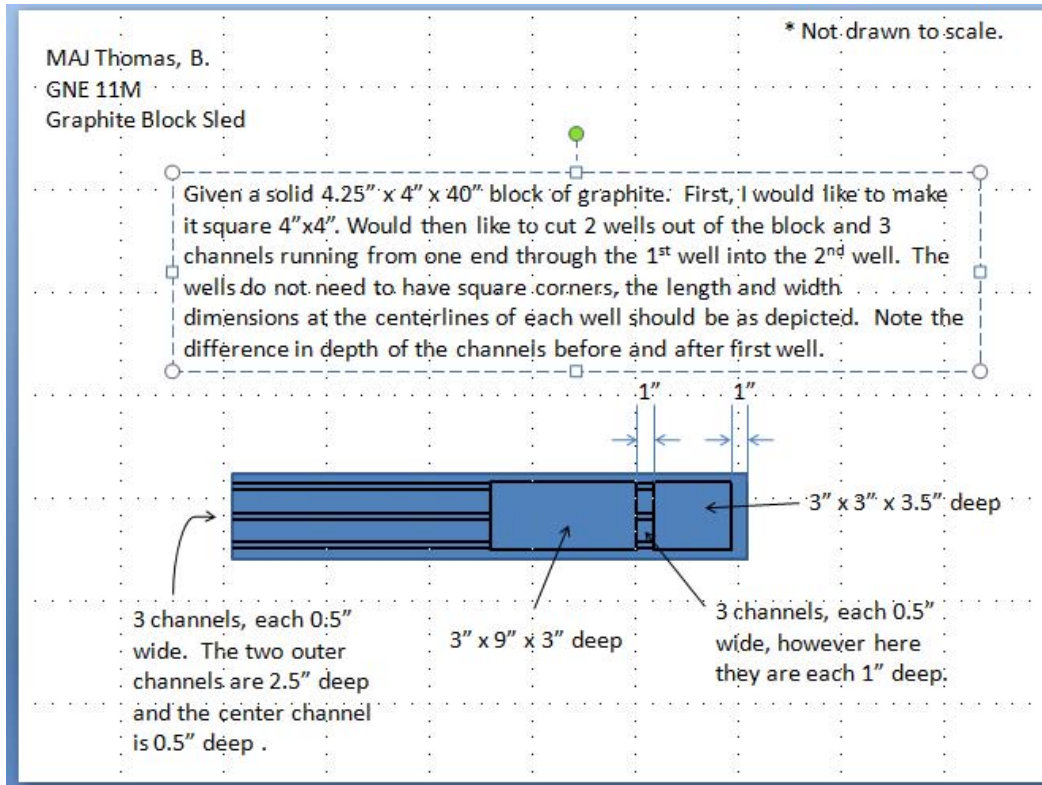
Appendix D – Test Fixture Designs

* Not drawn to scale.

MAJ Thomas, B.
GNE 11M
Graphite Block Sled

Given a solid 4.25" x 4" x 40" block of graphite. First, I would like to make it square 4"x4". Would then like to cut 2 wells out of the block and 3 channels running from one end through the 1st well into the 2nd well. The wells do not need to have square corners, the length and width dimensions at the centerlines of each well should be as depicted. Note the difference in depth of the channels before and after first well.

1" 1"

3" x 3" x 3.5" deep

3 channels, each 0.5" wide. The two outer channels are 2.5" deep and the center channel is 0.5" deep .

3" x 9" x 3" deep

3 channels, each 0.5" wide, however here they are each 1" deep.

MAJ Thomas, B.
GNE 11M
Graphite Block Sled

* Not drawn to scale.

TOP

40"

1"

1"

4"

Well
3" x 9" x 3" deep

Well
3" x 3" x
3.5" deep

END

SIDE

Well
3" x 9" x 3" deep

Well
3" x 3" x
3.5" deep

4"

4"

4"
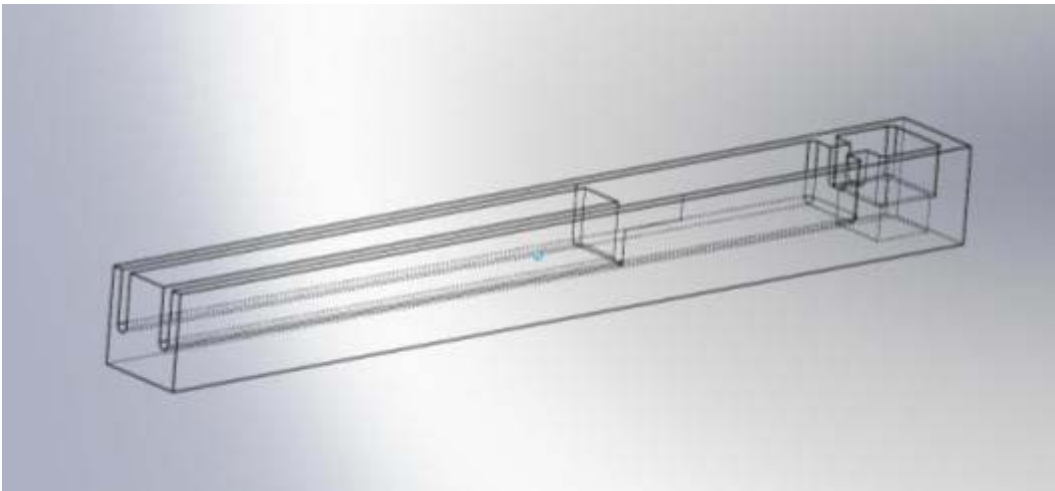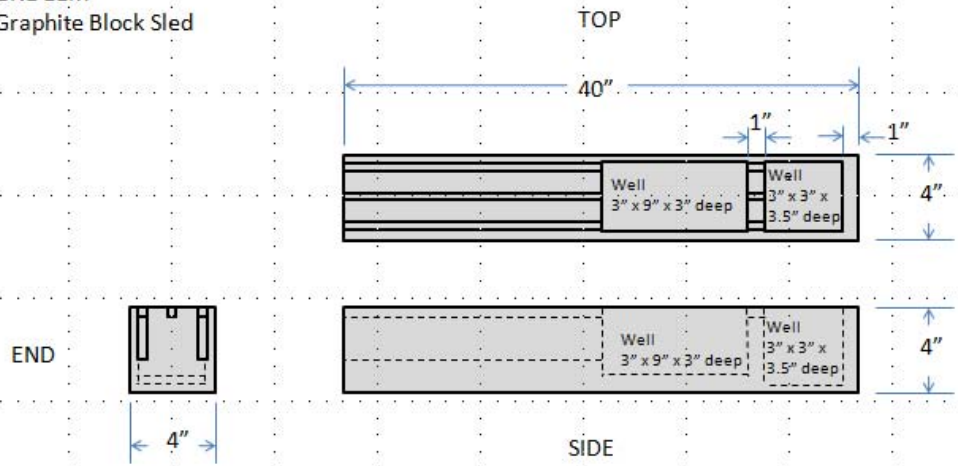
ENP/GNE 11M
Thomas, B
Diode Mount

Both pieces to made from 0.375" thick Lexan that I will provide. This first piece will be affixed to the part detailed on the next page with nylon bolts. Not sure of the bolt size, so I didn't mark the size of the 4 holes on this piece or the corresponding holes on the next piece.

1.50"

1.50"

1/3" x 1.00"

1" high x 1.5" long x 1/3" thick block on top of base to mount BNC connector.

1/16 deep etched out area

5/64 deep etched out area (1/64 deeper than the other etched out area)

2.95"

2.95"

¼" vent holes

82
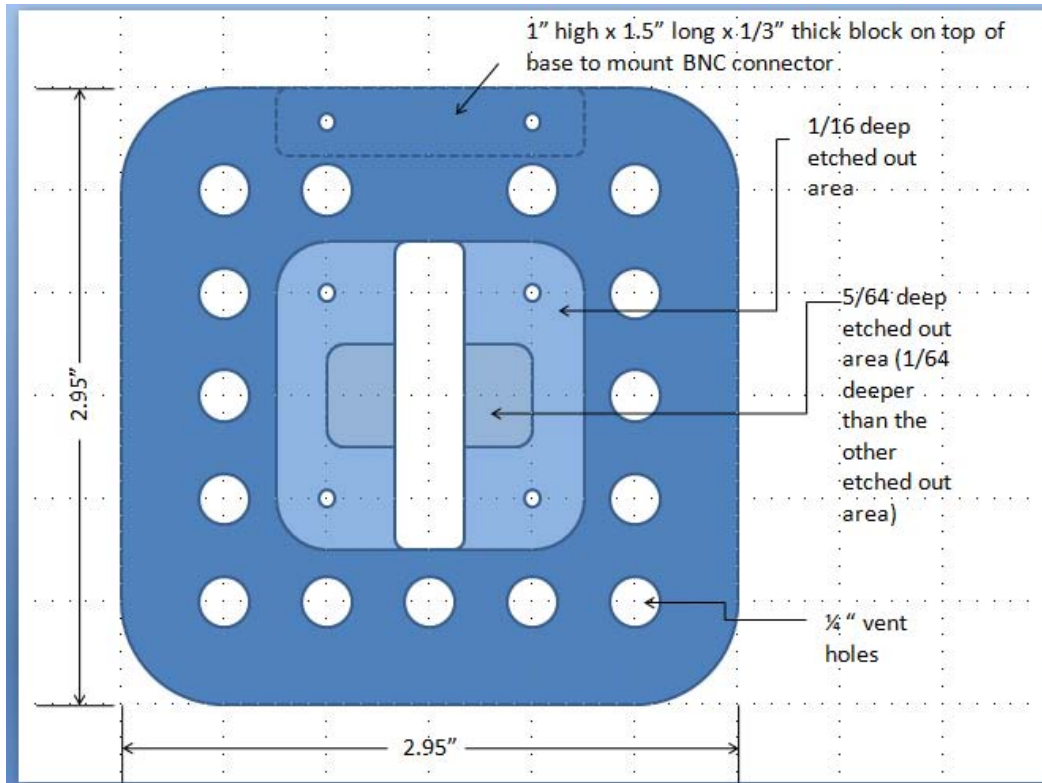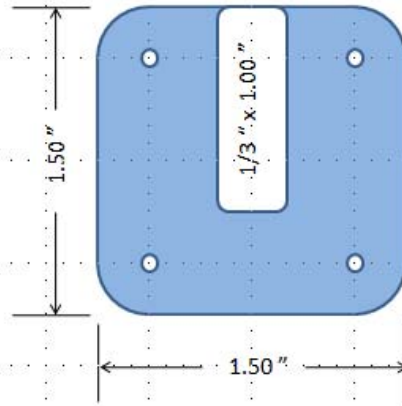
BIBLIOGRAPHY

[1]. Nuclear Regulatory Commission. *Special Nuclear Material.* http://www.nrc.gov/materials/sp-nucmaterials.html (accessed August 10, 2010).

[2]. C.J. Bridgman, *Introduction to the Physics of Nuclear Weapons Effects.* USA: Defense Threat Reduction Agency, 2001.

[3]. C. Young, "Gadolinium Oxide / Silicon Thin Film Heterojunction Solid-State Neutron Detector," MS thesis, Department of Engineering Physics, Air Force Institute of Technology, Wright-Patterson AFB, OH, 2010.

[4]. K.S. Krane, *Introductory Nuclear Physics*, New York: John Wiley and Sons, 1988.

[5]. K. Bird and M.J. Shermin. "Fallout." http://www.washingtonpost.com/ac2/wp-dyn/A35705-2005Apr7?language=printer (accessed June 21, 2010).

[6]. G.F. Knoll, *Radiation Detection and Measurement*, 3rd ed. Hoboken, NJ: John Wiley and Sons, 2000.

[7]. National Nuclear Data Center. *Evaluated Nuclear Data File (ENDF) Retrieval and Plotting.* http://www.nndc.bnl.gov/sigma/index.jsp (accessed July 15, 2010).

[8]. National Institute of Standards and Technology (NIST). *Atomic Weights and Isotopic Compositions for Gadolinium.* http://physics.nist.gov/cgi-bin/Compositions/stand_alone.pl?ele=Gd&ascii=html&isotype=all (accessed July 15, 2010).

[9]. M.A. Ali, V.A. Khitrov, A.M. Sokhovoj, and A.V. Vojnov, "Properties of the ^{158}Gd compound state Gamma-decay cascades", in *J. Phys. G: Nucl. Part. Phys.*, vol. 20, 1994, pp. 1943-1953.

[10]. M. Riordan, L. Hoddeson, *Crystal Fire: The Invention of the Transistor and the Birth of the Electronic Age.* New York, NY: W.W. Norton and Company, 1998 pp. 92-100.

[11]. M. Britt, *Pn Junction Equilibrium.svg* http://en.wikipedia.org/wiki/File:Pn_junction_equilibrium.svg (accessed December 21, 2010).

[12]. J.C. P*etrosky, "pn junction under* bias". NENG660:Radiation Effects on Electronics class notes issued to students, Air Force Institute of Technology, April 2010.

[13]. Y. Sakurai and T. Kobayashi, "Experimental Verification of the Nuclear Data of Gadolinium for Neutron Capture Therapy," *Nuclear Science and Technology*, sup. 2, Aug 2002, pp. 1294-1297.

[14]. Y.B. Losovyj, D. Wooten, J.C. Santana, J.M. An, K.D. Belashchenko, N. Lozova, J.C. Petrosky, A. Sokolov, J. Tang, W. Wang, N. Arulsamy, P.A. Dowben. "Comparison of n-type Gd_2O_3 and Gd-doped HfO_2." Journal of Physics: Condensed Matter, vol. 21, Jan 2009.

[15]. Spanish Inquisition 2006. *Configuration PLD.png* http://en.wikipedia.org/wiki/File:Configuration_PLD.png (accessed August 30, 2010).

[16]. S.M. Sze, *Semiconductor Devices, Physics and Technology*. Hoboken, NJ: John Wiley and Sons, 2002 pp. 84-129.

[17]. Ioffe Physico-Technical Institute. *Semiconductors on NSM Archive.* http://www.ioffe.ru/SVA/NSM//Semicond/SiC/index.html (accessed August 25, 2010).

[18]. D. Drouin, A.R. Couture, R. Gauvin, P. Hovington, P. Horny, H. Demers. "Monte Carlo Simulation of Electron Trajectory in Solids (CASINO)". Copyright 2001. Universite de Sherbrooke, Sherbrooke, Quebec, Canada. http://www.gel.usherbrooke.ca/casino/index.html (accessed June 21, 2010).

[19]. The Free Dictionary by Farlex, Gas Proportional Counter, http://encyclopedia2.thefreedictionary.com/Proportional+Counter (accessed November 12, 2010).

[20]. H. Pruchova, B. Franek, "3-Dimensional Simulation of Electron Avalanches in Low Pressure Wire Chambers and Proportional Counters." http://www.slac.stanford.edu/pubs/icfa/fall96/paper1/paper1/paper1.html (accessed November 12, 2010).

[21]. B. Van Zeghbroeck, "Principles of Semiconductor Devices."
http://ecee.colorado.edu/~bart/book/book/index.html (accessed December 16, 2010).

[22]. D. Defives, O.Durand, F. Wyczisk, O. Noblanc, C. Brylinski, F. Meyer, "Electrical Bevahiour and Microstructural Analysis of Metal Schottky Contacts on 4H SiC," in *Microstructural Engineering,* vol. 55, 2001, pp 369-374.

[23]. K. Jones, "Measurements of Neutron Induced Surface and Bulk Defects in 4H Silicon Carbide," MS Thesis, Department of Engineering Physics, Air Force Institute of Technology, Wright-Patterson AFB, OH, 2002.

[24]. C.A. Klein, "Bandgap Dependence and Related Features of Radiation Ionization Energies in Semiconductors," in *Journal of Applied Physics,* vol. 39, num. 4, March 1968. pp 2029-2038.

[25]. *Taurus Medici Davinci User's Guide*. Version Y-2006.06, Synopsis, Inc., June 2006.

[26]. *AF NETF Graphite Standard Pile,* Directorate of Engineering Test Aeronautical Systems Division, Air Force Systems Command, Wright-Patterson AFB, OH, Technical Document Report No. WAAD-T-61-174, March 1962.

[27]. J.P. McKelvey, *Solid State Physics for Engineering and Materials Science.* 2nd Edition, Malabar,FL: Kreiger Publishing Company, 2003.

[28]. M.Kobayashi, S.Sugimoto, Y. Yoshimura, Y. Usuki, M. Ishii, N. Senguttuvan, K. Tanji, M. Nikl,"A New Heavy and Radiation-Hard Cherenkov Radiator Based on $PbWO_4$," *Nuclear Instruments and Methods in Physics Research A*, vol. 459, 2001. pp 482-493.

[29]. D.Shultz, B.Blasy, J. Colon Santana, C.Young, J.C.Petrosky, J.W.McClory, D. LaGraffe, J.I.Brand, J.Tang, W.Wang, N.Schemm, S.Balkir, M.Bauer, I.Ketsman, R.W.Fairchild, Y.B.Losovyj, P.A.Dowben, "The K-Shell Auger Electron Spectrum of Gadolinium Obtained Using Neutron Capture in a Solid State Device," *Journal of Physics D: Applied Physics*, vol. 43, 2010.

[30]. B.Blasy, "Neutron Detection Utilizing Gadolinium Doped Halfnium Oxide Films," MS thesis, Department of Engineering Physics, Air Force Institute of Technology, Wright-Patterson AFB, OH, 2008.

REPORT DOCUMENTATION PAGE

1. REPORT DATE (DD-MM-YYYY)	2. REPORT TYPE	3. DATES COVERED (From - To)
25-03-2011	Master's Thesis	October 2010 – March 2011

4. TITLE AND SUBTITLE

Neutron Detection Using Gadolinium-Based Diodes

5a. CONTRACT NUMBER

5b. GRANT NUMBER

5c. PROGRAM ELEMENT NUMBER

6. AUTHOR(S)

Thomas, Benjamin R., MAJ, USA

5d. PROJECT NUMBER
na

5e. TASK NUMBER

5f. WORK UNIT NUMBER

7. PERFORMING ORGANIZATION NAME(S) AND ADDRESS(ES) AND ADDRESS(ES)

Air Force Institute of Technology
Graduate School of Engineering and Management (AFIT/EN)
2950 Hobson Way
Wright-Patterson AFB, OH 45433-7765

8. PERFORMING ORGANIZATION REPORT NUMBER

AFIT/GNE/ENP/11-M18

9. SPONSORING / MONITORING AGENCY NAME(S) AND ADDRESS(ES)

Defense Threat Reduction Agency
ATTN: Col. Mark Mattox
1900 Wyoming Blvd SE
Kirtland AFB, NM 87117-5669

10. SPONSOR/MONITOR'S ACRONYM(S)

DTRA/OP-CSU

11. SPONSOR/MONITOR'S REPORT NUMBER(S)

12. DISTRIBUTION / AVAILABILITY STATEMENT

APPROVED FOR PUBLIC RELEASE; DISTRIBUTION UNLIMITED

13. SUPPLEMENTARY NOTES

14. ABSTRACT
P-n heterojunction diodes consisting of a thin n-type layer of Gd_2O_3 deposited on both p-type Si and p-type 4H SiC substrates were explored as possible solid-state neutron detectors. 79 keV internal conversion electrons from the de-excitation of the meta-stable Gd-158 nucleus can create ionization in the depletion region of the reverse-biased diodes resulting in a detectable signal. The diodes were modeled with Davinci software to determine the feasibility of signal detection above the reverse-bias leakage current. A CASINO simulation showed that less than one percent of the internal conversion electrons deposit their full energy within the achievable depletion region. After depositing contacts on samples prepared at the University of Nebraska, Lincoln, the diodes were exposed to thermal neutron fluxes of approximately 10^3 n/cm^2·s in the AFIT Standard Graphite Pile and 10^9 n/cm^2·s in the thermal column of the Ohio State University Research Reactor. Pulse height spectra collected during irradiations at various reverse bias voltages ranging from -0.5 V to -5.0 V revealed no discernable neutron induced features. Oscilloscope traces captured during the high thermal neutron flux irradiations show pulses; however, no evidence exists to attribute these pulses to neutron interactions.

15. SUBJECT TERMS
Gadolinum Oxide, Gd2O3, Gadolina, Neutron Detection

16. SECURITY CLASSIFICATION OF:			17. LIMITATION OF ABSTRACT	18. NUMBER OF PAGES	19a. NAME OF RESPONSIBLE PERSON
a. REPORT U	**b. ABSTRACT** U	**c. THIS PAGE** U	UU	102	John W. McClory, LTC, USA
					19b. TELEPHONE NUMBER (include area code) (937) 255-3636, ext7308